



PRIFYSGOL CYMRU ABERTAWE  
UNIVERSITY OF WALES SWANSEA

**UNIVERSITY OF WALES SWANSEA**

***REPORT SERIES***

**Alternative subcell discretisations for viscoelastic flow:  
Velocity gradient approximation**

by

*F. Belblidia, H. Matallah and M. F. Webster*

Report # CSR 9-2007

 **Computer Science**  
**Gwyddor Cyfrifiadur**

## Alternative subcell discretisations for viscoelastic flow: Velocity gradient approximation

F. Belblidia, H. Matallah and M. F. Webster<sup>†</sup>

Institute of non-Newtonian Fluid Mechanics, Department of Computer Science,  
Swansea University, Singleton Park, Swansea, SA2 8PP, UK.

### Abstract

Under subcell discretisation for viscoelastic flow, we have given further consideration to the compatibility of function spaces for stress/velocity-gradient approximation (see [JNNFM, special issue AERC 2006]). This has been conducted through the three scheme discretisations (quad- $fe(par)$ ,  $fe(sc)$  and  $fe/fv(sc)$ ). In this companion study, we have extended the application of the original implementation for velocity gradient approximation, which was of localised superconvergent recovered form, continuous and quadratic on the parent  $fe$ -triangular element. This has led to the consideration of both localised (pointwise) and global (Galerkin weighted-residual) approximations for velocity gradients, highlighting some of their advantages and disadvantages. Each representation is based on linear/quadratic order upon parent or subcell element stencils. We consider Oldroyd modelling and the contraction flow benchmark, covering abrupt and rounded-corner planar geometries. The localised super-convergent quadratic velocity-gradient treatment affords strong stability and accuracy properties for the three scheme variants. Through associated analysis, we have successfully linked global approximations to their localised counterparts, depicting the inadequacy of inaccurate but stable versions through their corresponding solution features. The inaccuracy of the global treatment can be repaired through an increase in mass iteration number. The efficiency of localised schemes is particularly attractive over their global alternatives, being less restrictive to choice of spatial-order. Such schemes come into their own when chosen to represent strongly localised solution features, such as arise in non-smooth flows.

*Keywords:* viscoelastic, stability, subcell approximations, velocity gradients, localisation, global, recovery.

---

<sup>†</sup> Corresponding author. Tel: +44 1792 295656; fax: +44 1792 295708.  
*Email:* M.F.webster@swansea.ac.uk

## 1. Introduction

This article follows on from its precursor study concerned with the properties of subcell discretisations for viscoelastic flows [1]. There, we introduced a new subcell finite-element stress approximation within the framework of an incremental pressure-correction procedure, motivated by earlier successful hybrid finite element/volume implementations [2-4]. In [1], we focussed on the primary aspects of: compatibility of solution function spaces and implications on stress ( $\tau$ ) representation; finite element to finite volume spatial discretisation issues, covering upwinding choices in either context and improvements thereupon; enhancing stability upon the resulting variants via *Strain-rate Stabilisation*, see [5]. In this study, we particularly consider alternative choices under velocity gradient representation and their function space compatibility in the light of the foregoing study. This leads to consideration of both localised (pointwise-construction) and global (Galerkin weighted-residual) approximations for velocity gradients; continuous and of linear or quadratic order, upon both parent or subcell element reference. Tesselations are of triangular form, inherently unstructured, yet taken of somewhat regular form. The benchmark problem of contraction flow is retained, introduced earlier in [1], of both abrupt (non-smooth) and rounded-corner (smooth) varieties, oncemore subsuming the Oldroyd-B model for sake of consistency.

Under viscoelastic flows, the addition of a weak-form stress constitutive equation imposes supplementary compatibility conditions on admissible interpolation spaces for velocity-gradients ( $\nabla u$ ). It has been found sufficient for convergence that these fields should lie in finite dimensional spaces compatible with the choices selected for the primary stress variables, ( $S(\nabla u) \subset S(\tau)$ ) (extended Ladysenskaja-Babuska-Brezzi or *LBB* conditions, see Marchal and Crochet [6], Fortin and Fortin [7], Baaijens [8], re *DG*-schemes). The consequence of deviation from such conditions often appears in the form of numerical oscillations and poor stability response. The order of accuracy in representation for velocity-gradients plays a significant role in the satisfaction of such extended *LBB* conditions. Two main avenues have been developed for the treatment of velocity-gradients. The first approach is a localised treatment (based on either quadratic or linear interpolation, upon both parent or subcell element reference). The second approach is a global formulation which applies a weighted-residual approximation on the whole computational domain. Through both approaches, velocity gradients are considered as continuous derived fields (recovered, *VGR*). This is similar to the position under *Elastico-Viscous-Stress Splitting (EVSS)* schemes and their discrete (*DEVSS/SUPG*, *DEVSS/DG*) and adaptive (*AVSS/SI*, *AVSS/SUPG*) variants, see [7-12]). Through the choice of iterative solver employed for the global velocity gradient solution, we are able to draw upon theoretical identity for some localised approximations. This reveals their equivalence in stabilisation properties, but their deterioration in degree of accuracy under

mass lumping. We are able to pinpoint the consequences of the lack of satisfaction of ‘*space-inclusion extended LBB-condition*’ on some velocity gradient/stress combinations. The satisfaction of such conditions is also identified. This has ramifications for both pressure-correction and coupled-system formulations, such as those commonly quoted under *DEVSS*-variants, see Baaijens [8,12].

In Webster and co-workers [9,13], both local and global schemes were analysed and compared. There, a direct method was based on averaging of the velocity gradient contributions at a node over the elements in which it lies. For midside nodes, this provides superconvergent properties. The global Galerkin approach alternatively fits an appropriate set of nodal gradient values that satisfy an associated weighted residual formulation. A variant of this Galerkin method is based on an element-wise approximation and subsequent averaging. Hawken *et al.* [13] found that the local method offered better performance, for solution gradients in problems such as flow past a cylinder. Likewise, Matallah *et al.* [9] conducted similar analysis on a 4:1 contraction problem and flow around a cylinder, observing that the local recovery technique was more stable than a local Galerkin-equivalent. Much of this and similar work is summarised in Walters and Webster [14].

In previous study [1], we dealt with the localised approach alone and adopted a single approximation for velocity-gradients representation, that of localised superconvergent recovery cited in [9,13]. This interpolation is continuous and quadratic on the parent *fe*-triangular element. There, we analysed the effect of stress approximation through the implementation of three different interpolation schemes: *quad-fe(par)*, where we applied a quadratic stress approximation at the parent element level; and a subcell linear stress approximation, delivering two schemes, hybrid *fe/fv(sc)* and *fe(sc)* variants. Previous studies showed that the combination of quadratic interpolation for velocity-gradients on the parent element with the subcell linear approximation for stress within the constitutive equation grants a stable scheme, superior to that of its quadratic counterpart, whilst maintaining a second-third order of spatial convergence rate [1,15].

In the present study, we investigate the velocity gradient treatment under the same three schemes introduced earlier in [1], identified through their stress interpolation variants. Here, base form of such schemes is retained, that is: *SUPG-quad-fe*, *SUPG-fe(sc)* and *LDB-fe/fv(sc)*, see reference [1] for notational detail<sup>1</sup>. In Table I, we categorised variable interpolation, order selection and element reference with respect to these base-schemes. Careful attention has been given to the order of interpolation of stress and velocity gradients. Originally in [1], quadratic velocity gradient interpolation was considered on the parent element, regardless of the order of stress interpolation (being quadratic on the parent or linear on the subcell). In the present study and in addition to the original velocity-gradient interpolation described

---

<sup>1</sup> *SUPG*, streamwise upwind Petrov-Galerkin, *fe*-formulation; *LDB*, low diffusion B-scheme, *fv*-formulation.

above, we consider a linear velocity-gradient approximation on the subcell, alongside its related subcell linear stress interpolation.

We consider, as in [1], both non-smooth and smooth problem settings, adopting planar flow for an Oldroyd-B fluid in either sharp or rounded-corner 4:1 planar contractions. A schematic representation of the geometry, problem specification and boundary conditions are provided in Fig. 1, alongside a localised corner zoom to illustrate mesh quality around the contraction zone. Under the rounded-corner contraction setting ( $R=2/3$ , rounding), we are able to isolate the consequence of lip-vortex removal, in contrast to sharp-corner solutions. Extensive mesh refinement analysis has been conducted elsewhere under both problem configurations [1,3,16], where accuracy through mesh convergence was established. For the 4:1 contraction problem, the literature abounds with data on vortex behaviour, a fact that we exploit in our reporting of results. On the numerical side, relevant predictions have also been performed by Renardy [17], Oliveira and co-workers [18,19], and Webster and co-workers [3,5,20]. On the experimental side, related results are reported in Evans and Walters [21,22], Boger [23], and more recently, by McKinley and co-workers [24,25]. We have extensively investigated this problem in our recent work relating to the quad-*fe*(par) scheme [16]. Further analysis on the *fe/fv*(sc)-scheme has been explored in [1,5]. In all such studies under a sharp-corner setting and an Oldroyd-B model, we observe inhibition in salient-corner vortex intensity with increasing elasticity, and enhancement of the lip-vortex whenever present.

## 2. Governing equation and numerical algorithms

To specify the problem and under the assumption of isothermal, viscoelastic, incompressible fluid flow, the constitutive equation (CE) for stress may be expressed for the Oldroyd-B model as:

$$We \frac{\partial \boldsymbol{\tau}}{\partial t} = 2\mu_1 \mathbf{D} + \boldsymbol{\tau} - We(\mathbf{u} \cdot \nabla \boldsymbol{\tau} - \boldsymbol{\tau} \cdot \nabla \mathbf{u} - (\boldsymbol{\tau} \cdot \nabla \mathbf{u})^T), \quad (1)$$

where  $\mathbf{u}$  and  $\boldsymbol{\tau}$  represent velocity, and extra-stress, respectively. Total stress may be segregated into viscous and elastic parts,  $\mathbf{T} = 2\mu_2 \mathbf{D} + \boldsymbol{\tau}$ , and the rate-of-deformation is defined through the velocity gradient,  $L_u^T = \nabla \mathbf{u}$ , as:  $\mathbf{D} = (L_u + L_u^T)/2$  (boxed in Eq(1)). The zero shear viscosity is divided into polymeric ( $\mu_1$ ) and viscous ( $\mu_2$ ) contributions and  $We$  is the dimensionless Weissenberg number. Under weighted-residual approximation, *fe* or *fv*, the fully discrete equivalent CE for stress is extracted as expressed in [1]. For example, to extract a general term as for  $\boldsymbol{\tau} \cdot \nabla \mathbf{u}$  in a *fe*-framework, we first define the SUPG-weighting:

$$\omega_j = \begin{cases} \phi_j + \alpha^h \mathbf{u} \cdot \nabla \phi_j, & j=1,6 \quad (\text{par-quadratic}) \\ \psi_k + \alpha^h \mathbf{u} \cdot \nabla \psi_k, & k=1,3 \quad (\text{sc-linear}) \end{cases} \quad (2a)$$

$$\int_{\Omega} \chi(x) [\boldsymbol{\tau} \cdot \nabla u] d\Omega = \int_{\Omega} \chi(x) [\boldsymbol{\tau} \cdot L_u^T] d\Omega \rightarrow \int_{\Omega} \chi_i(x) [\boldsymbol{\tau}_j \omega_j^1(x)] \cdot [L_u^j \omega_j^2(x)] d\Omega .$$

According to the choice of the stress weighting ( $\chi_i$ ), the interpolation functions ( $\omega_j^1, \omega_j^2$ ) and domain space, we gather the various alternatives discussed below. Note, *fv*-weighting utilises a constant function in space (unity). In the present study, we appeal to extracted nodal values for the velocity-gradient and rate of deformation, that we employed directly within the discrete CE for stress. The nodal values for the rate of deformation may be expressed in a planar frame of reference as,

$$G_{k_1 k_2}(\mathbf{x}) = \frac{1}{2} \left\{ \frac{\partial u_{k_1}}{\partial x_{k_2}} + \frac{\partial u_{k_2}}{\partial x_{k_1}} \right\}, \quad k_1 = 1, 2; \quad k_2 = 1, 2 . \quad (2b)$$

This may be approximated in either a localised (*L*) or global (*G*) manner, implemented on the parent-element based on quadratic interpolation (*Quad-VGR-L*), or linear interpolation (*Lin-VGR-L*) applied to subtended subcell constructs.

### 2.1 Local velocity gradient treatment: *Quad-VGR-L* and *Lin-VGR-L*

Locally, and considering the area of each element involved in the evaluation of velocity-gradient components (see Fig. 2), two interpolation forms are offered for local, recovered velocity-gradients. The first is based on a quadratic interpolation on the parent element (*Quad-VGR-L*), compatible with both quadratic (*quad-fe(par)*) and subcell linear (*fe/fv(sc)*, *fe(sc)*) stress approximations. Currently, findings of earlier study [1] are recalled. The second alternative is a linear velocity-gradient form (*Lin-VGR-L*) which is compatible with the linear subcell stress variants (*fe/fv(sc)*, *fe(sc)*). The generalised local (pointwise-construction) approximations are of area-weighting form to account for departure from mesh uniformity. Simplified forms emerge under the assumption of mesh uniformity. Once nodal velocity-gradient values have been extracted, the two-stage recovery procedure [9] utilises the appropriate *fe*-basic functions to construct *C*<sup>0</sup>-*VGR*-representation.

#### 2.1.1 Quadratic, area-weighting:

We first provide the formulation for a quadratic velocity-gradient interpolation on the parent element, expressed under evaluation at node *i*:

$$G_{k_1 k_2}^i(\mathbf{x}) = \frac{\sum_{e=1}^{N_p} \Omega_e^i \left( \sum_{j=1}^6 \frac{1}{2} \left\{ \frac{\partial \phi_j}{\partial x_{k_2}} U_{k_1}^j + \frac{\partial \phi_j}{\partial x_{k_1}} U_{k_2}^j \right\} \right)^e}{\sum_{e=1}^{N_p} \Omega_e^i}, \quad (3)$$

where  $\Omega^i = \sum_{e=1}^{N_p} \Omega_e^i$ ,  $\Omega_e^i$  is a parent triangular element attached to node  $i$ , of number  $N_p$  over its compact support, with quadratic basis functions  $(\phi_j(x), j=1,6)$ .

### 2.1.2 Linear, area-weighting:

At this junction, the subcell format is employed, with stress and velocity-gradient being both linear. In this instance, the area of the subcell element is  $\Omega_{sc}$  and  $N_{sc}$  is the number of subcells surrounding node  $i$ , with linear basis functions  $(\phi_k(x), k=1,3)$ . Expression (3) is adjusted accordingly, viz.

$$G_{k_1 k_2}^i(\mathbf{x}) = \frac{\sum_{e=1}^{N_{sc}} \Omega_{sc}^i \left( \sum_{j=1}^3 \frac{1}{2} \left\{ \frac{\partial \psi_j}{\partial x_{k_2}} U_{k_1}^j + \frac{\partial \psi_j}{\partial x_{k_1}} U_{k_2}^j \right\} \right)^e}{\sum_{e=1}^{N_{sc}} \Omega_{sc}^i}. \quad (4)$$

Note that if  $\psi_j(\mathbf{x})$  is linear:  $\psi_j(\mathbf{x}) = \alpha_0^j + \alpha_{k_1}^j x_{k_1} + \alpha_{k_2}^j x_{k_2}$ ; thus, its derivatives are constants ( $\partial \psi_j / \partial x_{k_1} = \alpha_{k_1}^j = \text{cst}$  and  $\partial \psi_j / \partial x_{k_2} = \alpha_{k_2}^j = \text{cst}$ ). If the triangular elements (parents or subcells) surrounding a node are all of the same size, both quadratic and linear area-weighting formulae simplify (avoids area weighting) to:

$$G_{k_1 k_2}^i(\mathbf{x}) = \frac{\sum_{e=1}^{N_p} \left( \sum_{j=1}^6 \frac{1}{2} \left\{ \frac{\partial \phi_j}{\partial x_{k_2}} U_{k_1}^j + \frac{\partial \phi_j}{\partial x_{k_1}} U_{k_2}^j \right\} \right)^e}{N_p}, \quad (5a)$$

with  $\Omega^i = \sum_{e=1}^{N_p} \Omega_e^i = N_p \Omega_e^i$  for quadratic representation, or

$$G_{k_1 k_2}(\mathbf{x}) = \frac{\sum_{e=1}^{N_{sc}} \left( \sum_{j=1}^3 \frac{1}{2} \left\{ \frac{\partial \psi_j}{\partial x_{k_2}} U_{k_1}^j + \frac{\partial \psi_j}{\partial x_{k_1}} U_{k_2}^j \right\} \right)^e}{N_{sc}} = \frac{\sum_{e=1}^{N_{sc}} \left( \sum_{j=1}^3 \frac{1}{2} \{ \alpha_{k_2}^j U_{k_1}^j + \alpha_{k_1}^j U_{k_2}^j \} \right)^e}{N_{sc}} \quad (5b)$$

with  $\Omega^i = \sum_{e=1}^{N_{sc}} \Omega_e^i = N_{sc} \Omega_{sc}^i$  for linear representation. Typically, the evaluation of expression (5b) for one component (say  $(k_1, k_2) = (x, x)$ ) simplifies to:

$$G_{k_1 k_2}^i = \frac{\sum_{e=1}^{N_{sc}} \left( \sum_{j=1}^3 \frac{\partial \psi_j}{\partial x} U^j \right)^e}{N_{sc}} = \frac{\sum_{e=1}^{N_{sc}} \left( \sum_{j=1}^3 \alpha_1 U^j \right)^e}{N_{sc}}, \quad (6)$$

say, with  $x_{k_1} = x$  and  $U_{k_1} = U$ . We continue with this component choice and notation below.

## 2.2 Global velocity gradient treatment: Quad-VGR-G and Lin-VGR-G

Under the global treatment, the algebraic statement of the problem for velocity-gradients may be solved either by direct or iterative procedures. A direct approach is adopted under conventional *DEVSS*-implementations [7,8]. To suit present needs and analysis, we develop the use of an iterative approach via Jacobi-iteration. Under various settings, this permits access to theoretical counterparts to localised solutions (under a single iterative sweep, mass-lumping), as well as those gradually approaching the iterative converged-state for global domain-based forms (based on, say, five iterative sweeps and higher). The algebraic problem may be expressed according to the interpolation employed as:

$$M G = b, \quad (7a)$$

or, in the first component ( $xx$ ) form over row  $i$ , column  $j$ ,

$$(M_{ij})(G_{xx}^j) = (b_i). \quad (7b)$$

A Jacobi iterative solution procedure under iteration number  $r$  identifies iteration components,  $G_{xx}^r$ , and diagonalised preconditioner,  $(M_{ij})^d$ , viz.

$$G_{xx}^{r+1} = [M^d]^{-1} b + \left( I - [M^d]^{-1} M \right) G_{xx}^r. \quad (8)$$

The assembled mass matrix  $M$  is gathered from the elemental mass matrix contributions  $M^e$ , via the global Boolean transformation matrices,  $L_e$ , and the element sum,

$$M = \sum_{e=1}^{N_{elm}} L_e M^e L_e^T. \quad (9)$$

A similar assembly procedure applies equally to elemental contributions  $b^e$  for the right-hand-side  $b$ -vector, and likewise to the diagonal mass matrix  $M^d$ .

Considering elemental contributions (pre-assembly), and according to the interpolation employed through the selected scheme, components of matrix  $M^e$  and right-hand-side vector  $b^e$  may be expressed as:

$$M_{ij}^e = \begin{cases} \int_{\Omega_e} \phi_i \phi_j d\Omega & (\text{quad-fe}), \\ \int_{\Omega_{sc}} \psi_i \psi_j d\Omega & (\text{subcell}), \end{cases} \quad \text{and} \quad b_i^e = \begin{cases} \int_{\Omega_e} \phi_i \frac{\partial \phi_j}{\partial x} d\Omega U^j & (\text{quad-fe}), \\ \int_{\Omega_{sc}} \psi_i \frac{\partial \psi_j}{\partial x} d\Omega U^j & (\text{subcell}). \end{cases} \quad (10)$$

Next, we establish the triangular elemental left-hand side mass matrices for both linear interpolation schemes<sup>2</sup>,  $fe(sc)$  and  $fe/fv(sc)$ , followed by the right-hand-side terms. Mass matrices are,

$$(M^e)_{fe(sc)} = \frac{\Omega_{sc}}{12} \begin{bmatrix} 2 & 1 & 1 \\ 1 & 2 & 1 \\ 1 & 1 & 2 \end{bmatrix}, \quad (M^e)_{fe/fv(sc)} = \frac{\Omega_{sc}}{3} \begin{bmatrix} 1 & 1 & 1 \\ 1 & 1 & 1 \\ 1 & 1 & 1 \end{bmatrix}. \quad (11a)$$

We note that the direct elemental  $fe/fv(sc)$  mass matrix would deliver a singular system and this demands some form of preconditioning to yield a nodal solution, such as diagonalisation, or equivalently, Median-Dual-Cell (MDC) treatment [4,15] (see below). To extract preconditioners per scheme for iteration (8), we proceed with diagonalisation, in row-sum form to enhance iterative conditioning [15], yielding

$$(M^e)^d_{fe(sc)} = \frac{\Omega_{sc}}{12} \begin{bmatrix} 4 & 0 & 0 \\ 0 & 4 & 0 \\ 0 & 0 & 4 \end{bmatrix} = \frac{\Omega_{sc}}{3} \begin{bmatrix} 1 & 0 & 0 \\ 0 & 1 & 0 \\ 0 & 0 & 1 \end{bmatrix}, \quad (M^e)^d_{fe/fv(sc)} = \frac{\Omega_{sc}}{3} \begin{bmatrix} 3 & 0 & 0 \\ 0 & 3 & 0 \\ 0 & 0 & 3 \end{bmatrix} = \Omega_{sc} \begin{bmatrix} 1 & 0 & 0 \\ 0 & 1 & 0 \\ 0 & 0 & 1 \end{bmatrix}. \quad (11b)$$

Correspondingly, we consider right-hand-side terms,  $b_i^e$ , and note the constant nature of gradients on the subcell, of value  $(\alpha_k^j)$ . Furthermore, the weighting for  $fe/fv(sc)$  is unity ( $\psi_i = 1; i = 1,3$ ), which simplifies matters somewhat further. The resultant elemental right-hand side terms for  $fe(sc)$  and  $fe/fv(sc)$  are, respectively,

$$(b_i^e)_{fe(sc)} = \frac{\Omega_{sc}}{3} \begin{bmatrix} 1 \\ 1 \\ 1 \end{bmatrix} \sum_{j=1}^3 \alpha_k^j U^j, \quad (b_i^e)_{fe/fv(sc)} = \Omega_{sc} \begin{bmatrix} 1 \\ 1 \\ 1 \end{bmatrix} \sum_{j=1}^3 \alpha_k^j U^j. \quad (11c)$$

If we now consider iteration (8), under mass lumping (one iteration), with  $r=0$  and initial guess  $G_{xx}^0 = 0$ , then  $M^d G_{xx}^1 = b$  for the first base iterate,  $G_{xx}^1$ . Hence, considering elemental contributions per scheme,

---

<sup>2</sup> Based on,  $\int_{\Omega_{sc}} \psi_i^2 d\Omega = 2\Omega_{sc} \frac{2!}{(2+2)!} = \frac{\Omega_{sc}}{6}$ ;  $\int_{\Omega_{sc}} \psi_i \psi_j d\Omega = 2\Omega_{sc} \frac{1!}{(2+2)!} = \frac{\Omega_{sc}}{12}$ ;  $\int_{\Omega_{sc}} \psi_i d\Omega = 2\Omega_{sc} \frac{1}{3!} = \frac{\Omega_{sc}}{3}$ .

$$\left( \frac{\Omega_{sc}}{3} \begin{bmatrix} 1 & 0 & 0 \\ 0 & 1 & 0 \\ 0 & 0 & 1 \end{bmatrix} \right) (G_{xx}^1)_{fe(sc)} = \left( \frac{\Omega_{sc}}{3} \begin{bmatrix} 1 \\ 1 \\ 1 \end{bmatrix} \sum_{j=1}^3 \alpha_k^j U^j \right), \quad (12a)$$

$$\left( \Omega_{sc} \begin{bmatrix} 1 & 0 & 0 \\ 0 & 1 & 0 \\ 0 & 0 & 1 \end{bmatrix} \right) (G_{xx}^1)_{fe/fv(sc)} = \left( \Omega_{sc} \begin{bmatrix} 1 \\ 1 \\ 1 \end{bmatrix} \sum_{j=1}^3 \alpha_k^j U^j \right). \quad (12b)$$

Thus, we identify the collapse of schemes to provide the equivalence,  $(G_{xx}^1)_{fe(sc)} \equiv (G_{xx}^1)_{fe/fv(sc)}$ , under the assumptions of row-sum mass lumping iteration for  $fe(sc)$  and MDC for  $fe/fv(sc)$ . As such,  $fe(sc)$  discretisation is exactly equivalent to  $fe/fv(sc)$  for global velocity gradient treatment (a general theorem, of wider application; proof above). Note that, these elemental expressions (12) also pinpoint identity with expression (6) of the *Lin-VGR-L* scheme. Hence, we are *theoretically* able to link *global approximations* to their *localised counterparts* via the iterative formalism (Corollary 1). Likewise, an equivalence may be established between Median Dual Cell (MDC) approximation and diagonalisation of the full  $fe/fv(sc)$  system (Corollary 2). One may observe that MDC approximation evaluates elemental integrals for mass matrix and right-hand side vector over the MDC-area ( $\Omega_{MDC} = \Omega_{sc}/3$ ). Hence, the following identity may be established between  $(M^e)_{MDC}^d$  and  $(M^e)_{fe/fv(sc)}^{dd}$ , when appealing to direct diagonal (*dd*) extraction for the later,

$$(M^e)_{MDC}^d = \Omega_{MDC} \begin{bmatrix} 1 & 0 & 0 \\ 0 & 1 & 0 \\ 0 & 0 & 1 \end{bmatrix} = \frac{\Omega_{sc}}{3} \begin{bmatrix} 1 & 0 & 0 \\ 0 & 1 & 0 \\ 0 & 0 & 1 \end{bmatrix} = (M^e)_{fe/fv(sc)}^{dd} = \frac{1}{3} (M^e)_{fe/fv(sc)}^d. \quad (13)$$

We identify below in section 4, the relationship between various iteration number sweeps and solution dependency (domain penetration-Corollary 3). By increasing the number of Jacobi iterations, more elements (rings) are incorporated within the calculation of the nodal *VGR-G*, leading to more accurate velocity gradient evaluation through domain penetration, with converged *VGR-G* solutions approaching those obtained through the (local) *Quad-VGR-L* treatment.

In this study and for consistency sake, we follow a similar pattern for presentation of results as in [1], exposing numerical findings based on alternative schemes and velocity gradient treatments. We report on critical levels of  $We$  ( $We_{crit}$ ) to which convergence could be maintained, stress profiles and contours at common selected  $We=2.5$  and at  $We_{crit}$ , *VGR*-fields and on vortex characteristics. We are also able to point to specific advantages of the localised velocity-gradient treatment in contrast to its global counterpart. We

commence with the analysis for the local treatment in section 3, followed in section 4 by the global approach.

### 3. Localised velocity gradient treatment

In this section, we introduce detailed findings on two localised velocity-gradient treatments (*VGR-L*), of quadratic (*Quad-VGR-L*) and linear (*Lin-VGR-L*) representations. The analysis of stress profiles and fields, velocity gradient fields and vortex behaviour is performed to judge the stability properties of the *VGR-L* treatment applied. We also investigate the effect of area-averaging and rounded-corner solutions.

#### 3.1 Sharp-corner solutions

The sharp-corner setting provides a useful link to categorise the role of the solution singularity upon different schemes, which exhibits a large stress rise localised to the corner.

*Stress profiles with increasing  $We$ :* First and based on no-area-averaging methodology, in Fig. 3, we observe the contrast of localised velocity-gradient treatments (*VGR-L*), of linear (on *sc*) and quadratic (on *par*) representation, across our three-base schemes. We recall our earlier results for *Quad-VGR-L* [1], which demonstrate that the subcell approach for stress is superior in high-elasticity attainment to that using the parent-element alone. Also, seeking solutions at  $We$  of 2.8 and above, we observe that  $fe(sc)$  shows enhanced properties above  $fe/fv(sc)$ , in the tighter capture of the corner stress-peak and its undershoot (first-dip beyond the corner).

Shifting attention in contrast to *Lin-VGR-L*, we gather significant further gains in enhanced stability, practically doubling levels of  $We_{crit}$  achieved with *Quad-VGR-L*. This is similar in findings observed in early work [1], to the results upon application of the *Strain-Rate-Stabilisation (SRS)* technique. At larger levels of  $We$  beyond three, we begin to see transmission of perturbations along the wall-profiles. The  $fe(sc)$ -form above  $fe/fv(sc)$ , restrains stress-peak values, dip-levels and second-peaks, which may be quantified at say  $We=4.0$ . This leads to a larger level of  $We_{crit}$  attained of 5.7 for  $fe(sc)$ , as opposed to 4.6 for  $fe/fv(sc)$ . In this extended  $We$ -range with rising  $We$ , we also observe that  $fe/fv(sc)$ -profiles begin to display increasingly more exaggerated oscillatory form, just prior to the second stress-peak. We proceed to investigate further the properties of these schemes below.

#### 3.2 Influence of area-averaging

In contrast to results of Fig. 3, we next consider the application of area-averaging on velocity-gradients. Under current meshes that are highly regular, this additional strategy is found to have little, if any, impact on solution smoothness up to  $We_{crit}=2.6$  and with the *Quad-VGR-L* case. With *Quad-VGR-L*

$fe(sc)$ , there is restriction on  $We_{crit}$  by one unit. To say more on this issue, we focus on *Lin-VGR-L*  $fe(sc)$  results which attain larger  $We$ -solutions, say at  $We=5.0$ , to detect that the first stress-peak is slightly larger with area-averaging, yet the second-peak (reflected) is reduced. Note that the position of this second-peak coincides with the change in mesh density observed near the boundary exit wall at  $x=24$ , a localised phenomenon. Levels of  $We_{crit}$  are consequently slightly lowered over non-area-averaging alternatives, through both  $fe(sc)$  and  $fe/fv(sc)$ -schemes. Under  $fe/fv(sc)$  and the extended  $We$ -range above three, we identify in stress-profiles that area-averaging has considerably damped oscillations just prior to the second stress-peak, present without area-averaging.

A detailed view of Fig. 4 draws out solution-profile adjustment in the vicinity of mesh-change, according to inclusion of area-weighting or not on velocity gradient stencils. This is most prominent at the larger level of  $We=4.5$  and with  $fe/fv(sc)$ ; the impact on  $fe(sc)$  is minimal. Clearly,  $fv$ -weighting is more sensitive than  $fe$ -counterpart over such averaging treatment of velocity-gradients. Upon this basis, we interrogate more closely solution states on the field without area-averaging, nevertheless commenting upon its inclusion. Stress fields corroborate across schemes for subcritical and critical  $We$ -solutions; differences with area-weighting go undetected on the field.

### 3.2.1 Stress and velocity gradients fields:

At selected  $We$ -level, only minor differences in stress field are detected between quadratic and linear velocity gradient interpolation forms (not shown). In addition, we observe no stress oscillations streamwise and crosswind at subcritical  $We$  for both velocity gradients approximations independent of scheme employed. For velocity gradient solutions and at  $We=2.5$  under *Quad-VGR-L*, fields are smooth, for both  $fe(sc)$  and  $fe/fv(sc)$  variants, as shown in Fig. 5. Furthermore, oscillatory-free *Quad-VGR-L*-fields are enjoyed up to their respective  $We_{crit}$  attained for each scheme alternative. Upon switching to the *Lin-VGR-L*-implementation and under both  $fe(sc)$  and  $fe/fv(sc)$  variants, we observe the emergence of oscillations at  $We=2.5$ , that worsen with rising  $We$  up to critical level. This occurs mainly streamwise, whilst travelling along the downstream wall. This feature under *Lin-VGR-L*-form proves responsible for transmission to the stress profiles, as shown earlier.

### 3.2.2 Vortex behaviour:

*VGR-L*-streamline patterns are displayed in Fig. 6 and there is no difference detected via area-averaging. Therefore oncemore, only findings without area-averaging are presented. *Quad-VGR-L* produces consistency with published solutions on vortex behaviour through rising  $We$  [5,18], both in terms of trends in salient-corner and lip-vortex size/intensity, for both  $fe(sc)$  and  $fe/fv(sc)$  scheme alternatives. *Lin-VGR-L*, in contrast and under  $fe(sc)$ , generates exaggerated (double-sized in contrast to *Quad-VGR-L*) salient-corner vortices in intensity, with strong magnification of the lip-vortex. Thus, stability gains are

played off against accuracy. There are similar observations made under the  $fe/fv(sc)$  scheme, with growth of lip-vortices and salient-corner vortices. Yet at this juncture, the lip-vortex is constrained in size and does not influence the salient-corner vortex quite as much (see on, to more critical solution levels). What is apparent is the strong influence of the corner singularity upon the *Lin-VGR* formulation for both stress interpolations. This is demonstrated even more emphatically at  $We$  levels tending to critical. So that, *Lin-VGR-L* particularly stimulates large lip-vortex activity, revealing elaborate large and separate lip and salient-corner vortices (at  $We=4.0$ ), and those that even merge (after  $We=4.0$ ). The strong influence of *Lin-VGR-L* on lip-vortex activity is responsible for the salient-corner vortex enhancement at larger elasticity levels, a fact sometimes reported for other fluid models in these circumstances. This motivates below a comparative study of smooth flow alternatives (say upon rounded-corner domains) to identify the role of the singularity upon the discretisation options.

### 3.3 Rounded-corner solutions

#### 3.3.1 Vortex behaviour:

The adjustment of the sharpness of the corner by rounding completely removes the lip-vortex solution feature, as depicted in Fig. 7. Now and under the  $fe(sc)$  scheme, we only observe salient-corner vortex suppression with increasing elasticity up to  $We=5.0$ . This trend is in keeping across velocity-gradient schemes, and similar to that for the sharp-corner with *Quad-VGR-L*. Yet, the *Lin-VGR-L* predictions still display over-exaggeration in contrast to *Quad-VGR-L*, of  $O(25\%)$ . At super-elevated  $We$ -levels ( $We>5.0$ ) attainable under *Lin-VGR-L* alone, salient-corner vortex intensity is observed to slowly enhance, as clearly illustrated in Fig. 7 for  $We=7.5$  and  $We=9.5$ . So, once again, the stronger stability properties attached to the linear form when the singularity is omitted, are retained up to the super-elevated critical level,  $We_{crit}=9.9$ .

#### 3.3.2 Stress profiles with increasing $We$ :

Fig. 8 illustrates the lower stress-peaks generated by the rounded-corner above the sharp-corner solutions at comparable  $We$ -levels, and the enhancement in  $We_{crit}$  accordingly. Precisely, for *Quad-VGR-L* the  $We_{crit}$  increase is 3.6 to 5.1 (two units), whilst with *Lin-VGR-L*, it is 5.7 to 9.9 (four units). There is a lowering of stress-peaks at larger  $We$ -levels under *Lin-VGR-L*, in contrast to *Quad-VGR-L*. In fact, we observe a plateau in stress-peak levels under *Lin-VGR-L* for  $We\geq 4.0$ , whilst stress-peak levels continue to increase under *Quad-VGR-L*. This allows the *Lin-VGR-L* form to double its level of critical  $We$  (to  $We_{crit}=9.9$ ). Beyond  $We=4.0$  and for both velocity-gradient alternatives, downstream wall-stress even exceeds that of the stress-peak. The build-up of stress after the corner along the downstream wall, conveys minor perturbations in profiles with the *Quad-* but not *Lin-VGR-L* version, although identical stress levels

are reached on the boundary wall at  $We=3.5$  and  $We=5.5$ , as depicted in Fig. 8b. These appear to be lessened over their sharp-corner counterparts, in keeping with stress-peak reduction. Nevertheless, such downstream oscillations are still apparent under the *Lin-VGR-L* implementation. For *Lin-VGR-L*, localised oscillations appear around  $x = 8$  units from the corner-front face (location of mesh-density change), which are noted to spread for  $We \geq 6.0$  (see Fig. 8a at  $We=9.5$ ).

### 3.3.3 Stress and velocity gradient fields:

In Fig. 9, stress and velocity gradient fields are provided at  $We=2.5$  and  $5.0$ . At the lower level of  $We=2.5$ , stress fields remain smooth streamwise and cross-stream under both velocity-gradient treatments. We note however with *Lin-VGR-L*, that we can detect minor oscillations at the tail of the corner-rounding. This is highlighted below by analysing the *VGR*-fields under *Lin-VGR-L*:  $\partial U/\partial x$  and  $\partial U/\partial y$  are non-smooth, close to the corner. On the contrary under *Quad-VGR-L* and at the same  $We$ -level of  $2.5$ , *VGR*-fields remain smooth, even for contours around the corner. For both *VGR-L*-variants and at  $We \geq 5.0$  (about critical for *Quad-VGR-L*), although stress fields remain smooth in the domain, oscillations become apparent whilst approaching the near-corner vicinity. These oscillations are more pronounced under *Lin-VGR-L*, as gathered from the *VGR*-fields. At this  $We$ -level (half way towards  $We_{crit}$  for *Lin-VGR-L*), the more significant oscillations cross-stream disperse further along the downstream wall.

After thoroughly investigating the localised *VGR-L* treatment, we turn our attention next to the global domain *VGR-G* approach, yet omitting rounded-corner data.

## 4. Global velocity gradient treatment

Under global weighted-residual treatment, as with localised approximation, there are two *VGR-G* choices available independent of scheme/stress interpolation employed, see Table I. These are: *Quad-VGR-G*, where the velocity-gradients are computed at the parent-element nodes, based on quadratic interpolation; and *Lin-VGR-G*, where the interpolation is linear on the subcell. Under global domain treatment, a principal objective is to demonstrate the theoretical capture of the localised version *Lin-VGR-L*, when we revert to row-sum mass-lumping. This statement holds for either *fe(sc)* or *fe/fv(sc)*-versions, noting the equivalence to *median-dual-cell fe/fv(sc)*-approximation [4,15]. In addition, two-iterative sweeps with one ring of inter-connection established between solution nodal variables beyond the principal evaluation node (vertex), is equivalent to a localised Galerkin approximation per node where only the local compact support contributes (Corollary 3). Addition of subsequent iterative sweeps expands the layers of rings for solution dependence, penetrating the system matrix further. For conciseness, we only analysed *fe*-schemes under both velocity-gradient implementations, with either parent quad-*fe(par)* or subcell *fe(sc)* forms. In practise, the *fe/fv(sc)* global implementation proves identical to the *fe(sc)*-form

with mass-lumping, as demonstrated above. Furthermore, under various settings and depending on the number of mass iterations selected, this allows access to theoretical counterparts in localised solutions (e.g. under a single iterative sweep, mass-lumping), as well as trends gradually approaching the converged state of global domain-based forms (based on, say, five iterative sweeps and higher).

#### 4.1 Five mass iterations

Under this iteration setting, we are essentially considering iterative converged solutions (see below). We refer to Table II for a comparative summary of scheme characteristics and solution properties at a common level,  $We=1.0$ . We also report levels of  $We_{crit}$  and draw distinction between the various degrees of solution smoothness and scheme failure.

##### 4.1.1 Influence of space inclusion for stress and VGR:

The principal feature lies in the state of *VGR*-fields of Fig. 10 at sub-critical  $We=2.0$ . We analyse the sufficiency condition [6] for space-inclusion  $\{S(\nabla u) \subset S(\tau)\}$  under the two relevant stress approximations (quad-*fe*(par) and *fe*(sc)), combined with three possible forms of velocity gradient representation (*Quad-VGR-G*(par), *Lin-VGR-G*(par)) on parent element and *Lin-VGR-G*(sc) on subcell reference. This yields six possible combinations  $(\nabla u, \tau)$  to analyse under the TGPC-stencil. In the present study, the use of velocity-gradient recovery provides  $C^0$ -representation compatible with that of stress, as in the Hermitian element study of [6]. Note that linear stress interpolation in the context of quadratic velocity interpolation on the same (parent) element is a well know violating function space combination, see [26,27].

Considering first identical element reference, *Quad-fe*(par) and *Quad-VGR-G*(par) treatment exposes a common *quadratic* interpolation for both *VGR*  $(\nabla u^{2,p})$  and stress on the *shared* parent element ( $\tau$ -*fe*(par)). Note, space inclusion with equal order and element may be interpreted in either direction, so that  $\{S(\nabla u) \equiv S(\tau)\}$ . The *VGR*-field at  $We=2.0$  is partially-smooth throughout the downstream domain, as depicted in Fig. 10a (right), resulting in oscillatory stress field patterns (streamwise with field penetration cross-stream, Fig. 10a (middle)). This demonstrates signs of system inconsistency (stable, but inaccurate) through the combination of function spaces afforded. Inspection of the corresponding stress profiles of Fig. 10a (left) reveals that with rising  $We$ -levels, stress-profiles manifest local oscillations that only slowly decline along the downstream boundary wall.

A second combination entails sub-cell reference only with linear order, *Lin-VGR-G*(sc)  $(\nabla u^{1,sc})$  and  $\tau$ -*fe*(sc)-variant. Under this arrangement, smooth profiles are extracted along the boundary wall, reaching a

‘constant non-oscillatory’ plateau per  $We$ , as depicted in Fig. 10b (left). This is similar to findings under the localised *VGR*-treatment, with either *Quad/Lin-VGR-L*. In addition, all post-corner stress-profile dips remain positive up to  $We_{crit}$ . Furthermore at  $We=2.0$ , the stress field (Fig. 10b, middle) and *VGR*-field (Fig. 10b, right) are smooth on the domain (without oscillation, streamwise or cross-stream). Hence, system consistency (stability and accuracy) is captured under such subcell linear interpolation for both *VGR* and stress. This is the optimum combination observed under global approximation.

The remaining possible combination under identical parent element of reference is of unequal approximation order. This applies second order interpolation for stress: *Quad-fe(par)* and a linear order for *VGR*: *Lin-VGR-G(par)*,  $(\nabla u^{1,p})$ , so that the *VGR* space is contained within the stress space:  $S(\nabla u) \subset S(\tau)$ . This combination completely failed to provide a converged solution at even the smallest level of  $We=0.1$  (Fig. 10c), resulting in a worst-case failure scenario. This is in line with the claim of sufficiency (alone) of the space inclusion condition, as in Marchal and Crochet [6]. That is not discounting the open possibility that space inclusion could also be inverted, so that inclusion itself is violated with this combination of function spaces.

Mismatch of element-base for stress and *VGR* has been found to worsen system instability. This situation intrinsically defies space inclusion (proof obvious), as corroborated through the combination of the *fe(sc)*-stencil for stress whilst maintaining *Quad-VGR-G(par)* form, conveying a mismatch in order and element reference. At subcritical  $We=2.0$ , this demonstrates even greater *VGR*-field pollution (Fig. 10d, right) than under *Quad-VGR-G(par)* and *Quad-fe(par)* (of Fig.10a, right). This state is now clearly apparent also in the stress field solution (Fig. 10b, middle) a worsened state over that for (Fig. 10a, middle). The solution state is designated as ‘strongly non-smooth’ in Table II, column 1. Stress profiles show that the position gradually worsens with rise in  $We$ . Note, this setting provides the only instance where stress order is one order lower than on velocity gradient (even on mismatching element reference), adding some strength to the above statement on the direction of containment of function spaces.

Alternatively, by switching to the linear velocity gradient approximation on the subcell, *Lin-VGR-G(sc)*  $(\nabla u^{1,sc})$ , with *quad-fe(par)*, this particular combination also completely failed to provide a converged solution at  $We=0.1$  (Fig. 10e). Such an approximation is also a mismatch in order and element reference – again resulting in a worst-case failure scenario.

Maintaining linear interpolation order and element mismatch, as for *Lin-VGR-G(par)*  $(\nabla u^{1,p})$  with *fe(sc)* combination, leads to system failure at  $We=0.1$  once again (Fig. 10f), replicating the completely unstable state.

This understanding would lie alongside perceived wisdom of practical experience; see Marchal and Crochet [28]. In their work on coupled formulations and rectangular elements, they also proposed  $fe$ -subcell linear as a stable interpolation of stress and velocity gradients (global-weak form), based on parent elements with bi-quadratic approximations on velocity. At this juncture, we emphasise that under matching element of reference and identical order, when space inclusion is satisfied, stability is gathered. Furthermore, quadratic order is seen to degrade accuracy when applied to the parent element. For illustration, we observe stability/accuracy under linear order ( $Lin$ - $VGR$ - $G(sc)$  and  $fe(sc)$ ), but only stability with quadratic order ( $Quad$ - $VGR$ - $G(par)$  and  $quad$ - $fe(par)$ ). Mismatch in element reference and unequal interpolation order based on the global  $VGR$  context, violates the sufficiency condition on space inclusion, and displays various degrees of system incompatibility/breakdown. This ranges from strongly non-smooth fields, with some essence of stability retention, to complete lack of stability. Strongly non-smooth solutions result with  $fe(sc)$  and  $Quad$ - $VGR$ - $G(par)$ , with strong disturbance distributed throughout the downstream flow section. Complete instability applies under  $quad$ - $fe(par)$  and  $Lin$ - $VGR$ - $G(par)$  or  $sc$ ). Consequently, only stable and accurate combinations  $(\nabla u, \tau)$  under identical element of reference and equal order are employed in the present study ( $Quad$ - $VGR$ - $G$  and  $quad$ - $fe(par)$  under parent element and  $Lin$ - $VGR$ - $G$  and  $fe(sc)$  under subcell-basis).

#### 4.1.2 Compatibility repair through recovery and/or strain-rate-stabilisation:

Under the global-context, we are now in a position to investigate the possible repair of system consistency, manifest through the various degrees of inaccuracy or stability explored in solutions discussed thus far. In particular, we may interrogate different aspects associated with  $DEVSS$ -implementations, appending Strain-Rate-Stabilisation ( $SRS$ ) via the momentum differed-correction term,  $\alpha(D - D_c)$ , see Belblidia et al. [1,5] for definition.

With each pair of  $(\nabla u, \tau)$ , we have three possible implementations in mind: no- $SRS$  combined with  $VGR$  treatment in the constitutive equation (CE), the direct scheme as above;  $SRS$  without velocity gradient recovery treatment in CE (equivalent to  $DEVSS$ ); and  $SRS$  joint with  $VGR$  in CE (to mimic  $DEVSS$ - $G$ ). The outcome of such options spans the columns of Table II, where interestingly comments on smoothness of solution apply at all  $We$ -levels, not only  $We_{crit}$ . Our prior experience with localised  $VGR$ -treatment [9], would indicate that inclusion of  $VGR$ , in one or either of the stress or momentum equation, is somewhat equivalent in practical stability properties inherited. An overview of Table II findings would indicate that *neither Recovery nor SRS seriously influence the state of system consistency*: hence, smooth, partially-smooth, strongly non-smooth, or unstable states stay largely unaffected when  $SRS$  and/or recovery is introduced. Possible exception to this statement is for the  $DEVSS$ -implementation on quad-

$fe(par)$  under *Quad-VGR-G*, where the partial field smoothness of *VGR* is not inherited by stress, resulting in smooth stress fields, with a penalty of lowering  $We_{crit}$  (to 1.4 from a position of 2.2, see Table II). At this juncture, global quadratic recovery in *VGR*, employed in CE alone or with CE and *SRS-momentum*, is responsible for degrading *VGR* (and therefore stress) fields to a partial-smoothness level, whilst elevating stability properties (to  $We_{crit}=2.6$ ). *DEVSS-G* also enhances stability, without repairing lack of solution smoothness; conversely, *DEVSS* degrades stability. Not unexpectedly, once smoothness of solution has been established (stable and accurate), as with  $fe(sc)$  under *Lin-VGR-G*, then *DEVSS-G* (or equally *DEVSS*) strategies are found to further compliment stability gains ( $We_{crit}$  rises marginally from 2.7 to 2.8).

A further realisation is that *SRS*-inclusion has little influence in suppressing cross-stream numerical diffusion, as previously suggested theoretically. This is apparent from stress fields: discontinuity capturing for the non-smooth corner solution is the current tangible gain – with lowering of stress-peaks and finer capture of post-corner stress-dips.

#### 4.2 Effect of iteration number

In this section, we highlight the influence of the iteration number employed within the *Lin-VGR-G* treatment, under a single stress scheme stencil of  $fe(sc)$ . Mass-lumping is often employed as a stabilisation technique. As shown in Fig. 11, we demonstrate the effect of reducing the iteration number, from five to one. This has a direct impact on the critical level of  $We$  attained ( $We_{crit}=5.5$  for *Miter*=1, in contrast to 2.7 for *Miter*-converged). For mass-lumping stabilisation and large  $We$ -solutions ( $We>3.0$ ), oscillations are introduced in downstream-wall stress-profiles. These are similar to those already observed under the localised linear treatment of velocity-gradients (*Lin-VGR-L*). Note, that wall stress-levels tend to reach a plateau along the wall, although profiles become increasingly more oscillatory with rise in  $We$ . These oscillations are completely removed by increasing *Miter* to five and beyond, to a limiting *Miter*-converged state. At the same time, the levels of stress-peak reached under *Miter*-converged at equitable  $We$ -levels are slightly elevated above those for *Miter*=1, with sharper capture of solution peaks and dips.

These comments are reflected also in stress and velocity gradient fields, as depicted in Fig. 11. Under  $fe(sc)$ -scheme and *Lin-VGR-G* treatment, stress fields at both levels of mass iterations (one versus *Miter*-converged), remain smooth at lower  $We$ -levels ( $We=2.0$ ), as a consequence of smooth velocity gradient fields. These findings are maintained under the *Miter*-converged configuration up to  $We_{crit}=2.7$ . Alternatively, under *Miter*=1 and at the larger  $We$ -level of 5.5, *VGR*-oscillations around the corner are transmitted along the wall. This is a feature that results in more oscillatory wall stress-profiles.

### 4.3 Vortex behaviour

Under *Quad-VGR-G-quad-fe(par)* and  $Miter=5$  at  $We=2.0$ , there is a miniscule lip-vortex presence as shown in Fig. 12, with a well-developed salient-corner vortex. This result is largely in keeping with the literature, and increasing Miter number only serves to tighten the agreement. The *Lin-VGR-G-fe(sc)*-variant under the same Miter setting (of five) has delivered a larger lip-vortex (by about thirteen times) in contrast to the *quad-fe(par)*-solution. Correspondingly, the salient-corner vortex is also larger. Indeed, this comparison made at  $We=2.0$ , demonstrates the sensitivity of the numerical scheme employed to the velocity-gradient treatment, and hence, the compatibility of function spaces employed thereby. Reassuringly, we also observe that larger Miter number solutions tend to the consensus solution.

Considering only *Lin-VGR-G-fe(sc)*-solutions and reduction of iteration number (Miter) from five to one, we observe from Fig. 12 that both lip and salient-corner vortices are over-exaggerated. We note that none of the  $Miter=1$  findings presented for the salient-corner vortex under the global treatment of *VGR* match those of our earlier work [1], or those published by Alves *et al.* [18] and others [5,19]. Through these stream function predictions, we are able to detect the vital importance of sufficiency of convergence in intermediate *VGR*-solutions. This is further supported through vortex trends at extended elasticity levels of  $We=5.5$ , under *fe(sc)* and  $Miter=1$ . As we have observed under the *Lin-VGR-L-fe(sc)*, there is merging of vortices (salient-corner and lip), producing an excessively large vortex intensity. We argue that these findings are strongly influenced by the numerical discretisation error introduced via *Lin-VGR-G* ( $Miter=1$ ).

### 4.4 Localise vs. global velocity-gradient treatment

At this point, we draw the various strands of the work together under comparison of localised and global velocity gradient approximation. First, we take the comparison over pointwise treatments under the *fe(sc)* stencil alone: *Quad-VGR-L* and *Lin-VGR-L*. As illustrated in Fig. 13a, we are able to identify the sharp capture of stress-profiles with the *Quad-VGR-L* version. Second, re global approximations we may interrogate the influence of mass-iteration number, and in so doing expose the quality of converged intermediate-step *VGR*-solutions. We observe that mass-lumping (one iteration) underestimates stress-solution profiles, in comparison to five-iteration solutions, a trend that continues similarly up to Miter-convergence (Fig. 13b). The one-iteration version is theoretically known to be equivalent to the pointwise *Lin-VGR-L* form (also *fe/fv(sc)* equivalent), and this fact is confirmed in the final column of the figure throughout the  $We$ -range (Fig. 13d).

When considering comparison between localised (pointwise-*Quad*) and global (Galerkin-*Lin*) approaches, we are able to detect that with sufficient pursuit of velocity-gradient convergence, global

schemes can reproduce the high precision of the quadratic local form (see Fig. 13c). There is ample evidence at this point of the benefits that result from the additional  $C^0$ -continuity of *VGR* and superconvergence property on triangles that *Quad-VGR-L* enjoys [9,29], alongside the localisation that is inherent. Clearly, when strictly local features are present in the problem, such as in *non-smooth* flows say about re-entrant corners, the localisation property may have a stronger role to play. Note, mass conservation is ensured throughout, independent of scheme and *VGR* treatment (with or without *SRS*).

In passing and with back-reference to section 4.1b, we summarise in Table III the position re the potential benefits derived under the *localised velocity gradient* treatment with *fe(sc)*. This is a position where solution smoothness was observed independent of localised *VGR* interpolation order (*Quad/Lin-VGR-L*). In our prior work [1,5], based on *Quad-VGR-L*, *SRS*-addition (*DEVSS-G*) was found to enhance stability properties and retain accuracy, with significant impact upon  $We_{crit}$  elevation (from 3.6 to 4.2, see Table III). There, the influence of *SRS*-inclusion at large  $We$  remained localised through the lowering of re-entrant corner stress-peaks. This lay in distinct contrast to the situation without *SRS*-treatment. Furthermore, *SRS* retains solution smoothness as depicted in Table III. The *DEVSS*-form provides less stability, as reported in [9]. Upon recasting with the *Lin-VGR-L*-version, we observe no significant gain in stability and accuracy from a position under no-*SRS*. In summary and due to overall field findings (streamfunction), we recommend employment of *Quad-VGR-L* approximation to achieve both stability and accuracy under *SRS*-treatment.

#### 4.5 Asymptotic behaviour and mesh refinement

In previous studies, we have conducted extensive spatial consistency analysis based on three levels of mesh refinement (M1, M2 and M3), see on [4,16,30]. Particularly, in [1] and under *fe(sc)* scheme and *Quad-VGR-L* treatment [1], where the use of M3-mesh was justified through the analysis and contrast against a more refined mesh M4. The combination of linear stress approximation with a quadratic velocity gradient recovery technique under a pointwise approach (*Quad-VGR-L*) has been found to maintain a second-third order spatial accuracy. In the present study and for completeness, we display in Fig. 14 consistency through solution asymptotes and mesh refinement (M1, M2 and M3, introduced in [1]) for the *fe(sc)* scheme and *Lin-VGR-G* treatment. Here, we consider  $\tau_{xx}$  fields at  $We=1.5$  along with contrast against *Quad-VGR-L* solutions of M3-mesh, for robust implementations only. This evidence justifies the choice of the refined M3-mesh, shown in Fig. 1, through the sufficient solution smoothness and resolution extracted thereupon. Moreover, at  $We=1.5$  and under M3-mesh (Fig. 14), *Lin-VGR-G* treatment under *fe(sc)* scheme captures the correct theoretical asymptotic trend, being  $5/9$  rate for velocity components and  $-2/3$  slope for stress. Interestingly, we observe that *Lin-VGR-G* is more sensitive to mesh refinement in achieving accuracy (see M1-M2 behaviour) in contrast to *Quad-VGR-L* (of [1]).

## 5. Conclusions

This investigation has highlighted some of the advantages and disadvantages of applying localised (pointwise) and global (Galerkin) approximations to velocity-gradient fields in the context of viscoelastic flow. In our prior companion paper, base-forms of relevant pressure-correction schemes were established, quad- $fe(par)$ ,  $fe(sc)$  and  $fe/fv(sc)$ , upon which this study has been constructed. The present work has proved successful in theoretically linking global approximations to their localised counterparts. Thereby, the inadequacy of inaccurate but stable versions may be appreciated, through their corresponding solution features. These issues pervade all formulations, coupled or pressure-correction, and in focusing on velocity-gradient approximation, also by implication universally to all discrete representations of stress.

The efficiency of localised schemes is particularly attractive over their global alternatives, as localisation offers little restrictions on choice of  $VGR$ -order of interpolation and potentially other benefits in tighter capture of local solution features (discontinuity capturing for non-smooth flows). We have been able to identify the favourable strong stability and accuracy properties afforded by the super-convergent quadratic velocity-gradient interpolation on the parent-element *localised* formulation ( $Quad-VGR-L$ ). The various alternative interpolation combinations offered prove less favourable in comparison; in particular, global forms and the localised linear velocity-gradient interpolation on the sub-element ( $Lin-VGR-L-fe(sc)$ ). This largely bears out the need (or not) for the satisfaction of the extended LBB-condition of space inclusion of Marchal and Crochet, and Fortin and Fortin. Experience has revealed that global- $VGR$  extraction is more restrictive in satisfaction of the space-inclusion principal: here only  $Lin-VGR-G$  with  $fe(sc)$  has proved stable and robust. Under localised- $VGR$  approximation, wider latitude is permissible: so that higher-order approximation (quadratic) may be realised and localised properties may be brought to bear, such as superconvergence. In addition and by design, these recovery techniques offer  $C^0$ -continuity on velocity gradients. Their localised nature makes these procedures more suitable for non-smooth flows. Loss of the superconvergence property may be appreciated through the  $Lin-VGR-L$  treatment. Overall, efficient localised formulations have been helpful in clarifying that space inclusion is a non-necessary convergence condition in the viscoelastic context.

With respect to aspects of detail relating to  $DEVSS$ -type implementations, we can comment that once function spaces for the principal variables of stress and velocity-gradients have been selected, that this choice rather dictates the state of system consistency. This is largely uninfluenced by recovery, or Strain-Rate Stabilisation, or their combination. Once stable and accurate solutions have been devised, only then can enhanced stability be engineered by such additional strategies. In addition, Strain-Rate Stabilisation proves itself to be particularly effective in its discontinuity capturing properties [3,5], pertinent therefore to non-smooth corner solution representation.

**Acknowledgements:** We gratefully acknowledge financial support under the EPSRC grant 'Complex Fluids and Complex Flows - Portfolio Partnership (EP/C513037)'

## References

- [1] F. Belblidia, H. Matallah, B. Puangkird and M.F. Webster, Alternative subcell discretisations for viscoelastic flow: Stress interpolation, *J. Non-Newtonian Fluid Mech.* (in press 2007).
- [2] P. Wapperom and M.F. Webster, A second-order hybrid finite-element/volume method for viscoelastic flows, *J. Non-Newtonian Fluid Mech.* **79** (1998) 405-431.
- [3] M. Aboubacar and M.F. Webster, A cell-vertex finite volume/element method on triangles for abrupt contraction viscoelastic flows, *J. Non-Newtonian Fluid Mech.* **98** (2001) 83-106.
- [4] M.F. Webster, H.R. Tamaddon-Jahromi and M. Aboubacar, Transient viscoelastic flows in planar contractions, *J. Non-Newtonian Fluid Mech.* **118** (2004) 83-101.
- [5] F. Belblidia, I.J. Keshtiban and M.F. Webster, Stabilised computations for viscoelastic flows under compressible implementations, *J. Non-Newtonian Fluid Mech.* **134** (2006) 56-76.
- [6] J.M. Marchal and M.J. Crochet, Hermitian finite elements for calculating viscoelastic flow, *J. Non-Newtonian Fluid Mech.* **20** (1986) 187-207.
- [7] M. Fortin and A. Fortin, A new approach for the FEM simulation of viscoelastic flows, *J. Non-Newtonian Fluid Mech.* **32** (1989) 295-310.
- [8] F.P.T. Baaijens, An iterative solver for the DEVSS/DG method with application to smooth and non-smooth flows of the upper convected Maxwell fluid, *J. Non-Newtonian Fluid Mech.* **75** (1998) 119-138.
- [9] H. Matallah, P. Townsend and M.F. Webster, Recovery and stress-splitting schemes for viscoelastic flows, *J. Non-Newtonian Fluid Mech.* **75** (1998) 139-166.
- [10] R. Guénette and M. Fortin, A new mixed finite element method for computing viscoelastic flows, *J. Non-Newtonian Fluid Mech.* **60** (1995) 27-52.
- [11] J. Sun, N. Phan-Thien and R.I. Tanner, An adaptive viscoelastic stress splitting scheme and its applications: AVSS/SI and AVSS/SUPG, *J. Non-Newtonian Fluid Mech.* **65** (1996) 75-91.
- [12] F.P.T. Baaijens, Mixed finite element methods for viscoelastic flow analysis: a review, *J. Non-Newtonian Fluid Mech.* **79** (1998) 361-385.
- [13] D.M. Hawken, P. Townsend and M.F. Webster, A comparison of gradient recovery methods in finite element calculations, *Comm. Appl. Num. Meth.* **7** (1991) 195-204.
- [14] K. Walters and M.F. Webster, The distinctive CFD challenges of computational rheology, *Int. J. Num. Meth. Fluids* **43** (2003) 577-596.
- [15] M.F. Webster, H.R. Tamaddon-Jahromi and M. Aboubacar, Time-dependent algorithm for viscoelastic flow-finite element/volume schemes, *Num. Meth. Partial Diff. Equ.* **21** (2005) 272-296.
- [16] I.J. Keshtiban, F. Belblidia and M.F. Webster, Numerical simulation of compressible viscoelastic liquids, *J. Non-Newtonian Fluid Mech.* **122** (2004) 131-146.
- [17] M. Renardy, Current issues in non-Newtonian flows: a mathematical perspective, *J. Non-Newtonian Fluid Mech.* **90** (2000) 243-259.

- [18] M.A. Alves, P.J. Oliveira and F.T. Pinho, Benchmark solutions for the flow of Oldroyd-B and PTT fluids in planar contractions, *J. Non-Newtonian Fluid Mech.* **110** (2003) 45-75.
- [19] P.J. Oliveira and F.T. Pinho, Plane contraction flows of upper convected Maxwell and Phan-Thien-Tanner fluids as predicted by a finite-volume method, *J. Non-Newtonian Fluid Mech.* **88** (1999) 63-88.
- [20] M. Aboubacar, H. Matallah, H.R. Tamaddon-Jahromi and M.F. Webster, Numerical prediction of extensional flows in contraction geometries: hybrid finite volume/element method, *J. Non-Newtonian Fluid Mech.* **104** (2002) 125-164.
- [21] R.E. Evans and K. Walters, Flow characteristics associated with abrupt changes in geometry in the case of highly elastic liquids, *J. Non-Newtonian Fluid Mech.* **20** (1986) 11-29.
- [22] R.E. Evans and K. Walters, Further remarks on the lip-vortex mechanism of vortex enhancement in planar-contraction flows, *J. Non-Newtonian Fluid Mech.* **32** (1989) 95-105.
- [23] D.V. Boger, Viscoelastic flows through contractions, *Annual Rev. Fluid Mech.* **19** (1987) 157-182.
- [24] L.E. Rodd, T.P. Scott, D.V. Boger, J.J. Cooper-White and G.H. McKinley, The inertio-elastic planar entry flow of low-viscosity elastic fluids in micro-fabricated geometries, *J. Non-Newtonian Fluid Mech.* **129** (2005) 1-22.
- [25] J.P. Rothstein and G.H. McKinley, Extensional flow of a polystyrene Boger fluid through a 4:1:4 axisymmetric contraction/expansion, *J. Non-Newtonian Fluid Mech.* **86** (1999) 61-88.
- [26] M. Kawahara and N. Takeuchi, Mixed finite element method for analysis of viscoelastic fluid flow, *Comput. & Fluids* **5** (1977) 33-45.
- [27] M.J. Crochet and G. Pilate, Numerical study of the flow of a fluid of second grade in a square cavity, *Comput. & Fluids* **3** (1975) 283-291.
- [28] J.M. Marchal and M.J. Crochet, A new mixed finite element for calculating viscoelastic flow, *J. Non-Newtonian Fluid Mech.* **26** (1987) 77-114.
- [29] O.C. Zienkiewicz and J.Z. Zhu, Superconvergence and the superconvergent patch recovery, *Finite Elem. Anal. Design* **19** (1995) 11-23.
- [30] I.J. Keshtiban, F. Belblidia and M.F. Webster, Computation of incompressible and weakly-compressible viscoelastic liquids flow: finite element/volume schemes, *J. Non-Newtonian Fluid Mech.* **126** (2005) 123-143.

**List of Tables**

Table I. Velocity-gradient treatment

Table II. Compatibility through momentum treatment, global VGR-G, Miter=5;  $We=1.0$

Table III. Compatibility through momentum treatment,  $fe(sc)$ , local VGR-L;  $We=2.0$

**Table I.** Velocity-gradient treatment

	VGR-L Local- ptwise		VGR-G Global-Galerkin		
	Quad-VGR-L $\nabla \mathbf{u}^{2,p}$	Lin-VGR-L $\nabla \mathbf{u}^{1,sc}$	Iter.	Quad-VGR-G $\nabla \mathbf{u}^{2,p}$	Lin-VGR-G $\nabla \mathbf{u}^{1,sc}$
$\tau-fe(par)$ $\tau^{2,p}$	$We_{crit} = 2.2$ <sup>1</sup>	Theoretically as Lin-VGR-G	Mass 1	-	-
			Mass 5	$We_{crit} = 2.2$ <sup>2</sup>	fail <sup>4</sup>
$\tau-fe(sc)$ $\tau^{1,sc}$	$We_{crit} = 3.6$ <sup>1</sup>	$We_{crit} = 5.7$ <sup>2</sup>	Mass 1	fail <sup>4</sup>	$We_{crit} = 5.5$ <sup>2</sup>
			Mass 5	$We_{crit} = 3.0$ <sup>3</sup>	$We_{crit} = 2.7$ <sup>1</sup>
$\tau-fe/fv(sc)$ $\tau^{1,sc}$	$We_{crit} = 2.8$ <sup>1</sup>	$We_{crit} = 4.6$ <sup>2</sup>			

<sup>(1)</sup> accurate and strongly stable

<sup>(2)</sup> partially smooth (mild perturbations in VGR, slight influence on stress-field)

<sup>(3)</sup> strongly non-smooth (major field perturbations in both VGR and stress)

<sup>(4)</sup> complete scheme failure

**Table II.** Compatibility through momentum treatment, global VGR-G, Miter=5;  $We=1.0$

	<i>Recov., no SRS (no treatment)</i>	<i>No Recov., SRS (DEVSS)</i>	<i>Recov., SRS (DEVSS-G)</i>
<i>Quad-VGR-G (<math>\nabla u^{2,p}</math>) - parent</i>			
$\tau$ -fe(par); $\tau^{2,p}$	stress <sup>2</sup> , VGR <sup>2</sup>	stress <sup>1</sup> , VGR <sup>2</sup>	stress <sup>2</sup> , VGR <sup>2</sup>
	$We_{crit} = 2.2$	$We_{crit} = 1.4$	$We_{crit} = 2.6$
$\tau$ -fe(sc); $\tau^{1,sc}$	stress <sup>3</sup> , VGR <sup>3</sup>	fail <sup>4</sup>	fail <sup>4</sup>
	$We_{crit} = 3.0$	-	-
<i>Lin-VGR-G (<math>\nabla u^{1,sc}</math>) - subcell</i>			
$\tau$ -fe(par); $\tau^{2,p}$	fail <sup>4</sup>	fail <sup>4</sup>	fail <sup>4</sup>
$\tau$ -fe(sc); $\tau^{1,sc}$	stress <sup>1</sup> , VGR <sup>1</sup>	stress <sup>1</sup> , VGR <sup>1</sup>	stress <sup>1</sup> , VGR <sup>1</sup>
	$We_{crit} = 2.7$	$We_{crit} = 2.8$	$We_{crit} = 2.8$
<i>Lin-VGR-G (<math>\nabla u^{1,p}</math>) - parent</i>			
$\tau$ -fe(par); $\tau^{2,p}$	fail <sup>4</sup>	-	-
$\tau$ -fe(sc); $\tau^{1,sc}$	fail <sup>4</sup>	-	-

<sup>(1)</sup> smooth, <sup>(2)</sup> partially smooth, <sup>(3)</sup> strongly non smooth, <sup>(4)</sup> complete scheme failure

Note: <sup>(1), (2), (3)</sup> at any  $We$ -level, <sup>(4)</sup>  $We=0.1$  not reached from quiescent state

**Table III.** Compatibility through momentum treatment,  $fe(sc)$ , local VGR-L;  $We=2.0$

	<i>Recov., no SRS (no treatment)</i>	<i>Recov., SRS (DEVSS-G)</i>	<i>Recov., no SRS (no treatment)</i>	<i>Recov., SRS (DEVSS-G)</i>
	<i>Quad-VGR-L (<math>\nabla \mathbf{u}^{2,p}</math>)</i>		<i>Lin-VGR-L (<math>\nabla \mathbf{u}^{l,sc}</math>)</i>	
$\tau-fe(sc); \tau^{l,sc}$	(stress profile, stress and VGR) <sup>1</sup>	(stress profile, stress and VGR) <sup>1</sup>	stress profile <sup>2</sup> , (stress, VGR) <sup>1</sup>	stress profile <sup>2</sup> , (stress, VGR) <sup>1</sup>
	$We_{crit} = 3.6$	$We_{crit} = 4.2$	$We_{crit} = 5.7$	$We_{crit} = 5.8$

<sup>(1)</sup> smooth, <sup>(2)</sup> partially smooth. Note: <sup>(1), (2)</sup> at any  $We$ -level

### List of Figures

- Fig. 1. Contraction flow problems: a) schema, b) mesh around contraction (sharp and rounded corner)
- Fig. 2. a) Parent  $fe$  and subcells tessellations; b)  $MDC$  area for node  $l$
- Fig. 3. Stress profiles, increasing  $We$ ;  $\tau_{xx}$ -profiles, downstream-wall; under (top)  $Quad-VGR-L$ , (bottom)  $Lin-VGR-L$ ; a) quad- $fe(par)$ , b)  $fe(sc)$  and c)  $fe/fv(sc)$ ; no-area averaging
- Fig. 4. Area-averaging (AA) vs. no-area-averaging (nAA), stress profiles,  $We=2.0, 2.5$  and  $4.5$ ;  $\tau_{xx}$ -profiles, downstream-wall; under a)  $fe(sc)-Quad-VGR-L$ , b)  $fe(sc)-Lin-VGR-L$  and c)  $fe/fv(sc)-Lin-VGR-L$
- Fig. 5. Velocity-gradient fields,  $We=2.5, We_{crit}$ ; (top)  $Quad-VGR-L$ , (bottom)  $Lin-VGR-L$ ; (left)  $fe(sc)$  and (right)  $fe/fv(sc)$
- Fig. 6. Vortex behaviour, increasing  $We$ ; (top)  $Quad-VGR-L$ , (bottom)  $Lin-VGR-L$ ; (left)  $fe(sc)$  and (right)  $fe/fv(sc)$
- Fig. 7. Vortex behaviour, increasing  $We$ ; (left)  $Quad-VGR-L$ , (right)  $Lin-VGR-L$ ;  $fe(sc)$ ; rounded-corner contraction
- Fig. 8. a) Stress profiles, increasing  $We$ ;  $\tau_{xx}$ -profiles, downstream-wall; under (left)  $Quad-VGR-L$ , (right)  $Lin-VGR-L$  with zoom window;
- Fig. 9. Stress and velocity-gradient fields, (top)  $We=2.5$  and (bottom)  $We=5.0$ ;  $fe(sc)$ ; under (left)  $Quad-VGR-L$ , (right)  $Lin-VGR-L$ ; rounded contraction
- Fig. 10. Stress profiles, increasing  $We$ ; stress and velocity-gradient fields,  $We=2.0$ ; under identical element-base, a)  $Quad-VGR-G(par)$ , quad- $fe(par)$ , b)  $Lin-VGR-G(sc)$ ,  $fe(sc)$ , c)  $Lin-VGR-G(par)$ , quad- $fe(par)$ ; element mismatch, d)  $Quad-VGR-G(par)$ ,  $fe(sc)$ , e)  $Lin-VGR-G(sc)$ , quad- $fe(par)$ , f)  $Lin-VGR-G(par)$ ,  $fe(sc)$ ; Miter=5
- Fig. 11. Stress profiles, increasing  $We$ ; stress and velocity-gradient fields,  $We=2.0$ ;  $fe(sc)$ ,  $Lin-VGR-G$ ; under (left) Miter=1, (right) Miter=converge
- Fig. 12. Vortex behaviour, increasing  $We$ ; (top) quad- $fe(par)$ ,  $Quad-VGR-G$ , (bottom)  $fe(sc)$ ,  $Lin-VGR-G$ ; under (left) Miter=1, (right) Miter=5
- Fig. 13. Various  $VGR$ -treatments,  $fe(sc)$ , stress profiles,  $We=2.0, 3.5$  and  $5.0$ ;  $\tau_{xx}$ -profiles, downstream-wall; under a)  $Quad-VGR-L/Lin-VGR-L$ , b)  $Lin-VGR-G1/Lin-VGR-Gcvg$ , c)  $Quad-VGR-L/Lin-VGR-Gcvg$ , d)  $Lin-VGR-L/Lin-VGR-G1$
- Fig. 14. Mesh refinement,  $fe(sc)-Lin-VGR-G$ ,  $We=1.5$ ; (top)  $\tau_{xx}$  and  $\partial U/\partial x$ -contour fields, a) mesh M1, b) M2 and c) M3; (bottom) asymptotic behaviour near re-entrant corner, (left) velocity ( $U, V$ ), (right) stress ( $\tau_{xx}, \tau_{xy}$ ), different meshes M1-M3



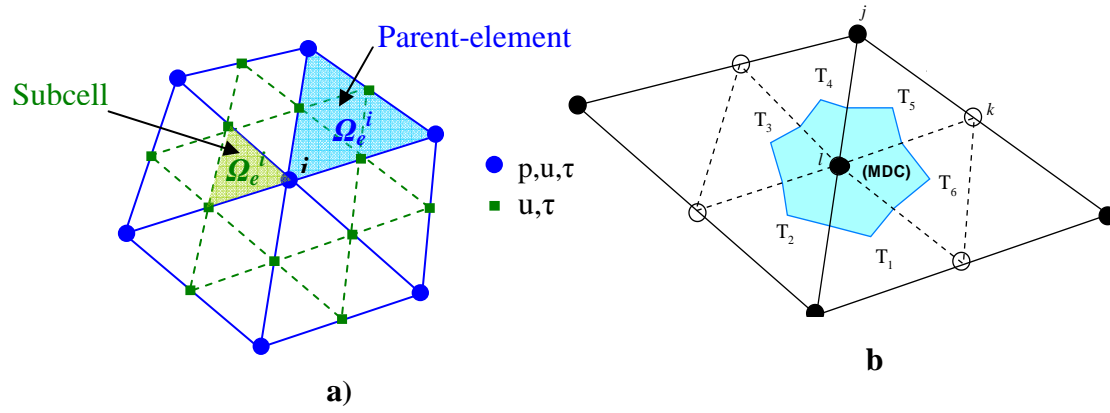


**Fig. 2.** a) Parent  $fe$  and subcells tessellations; b)  $MDC$  area for node  $l$

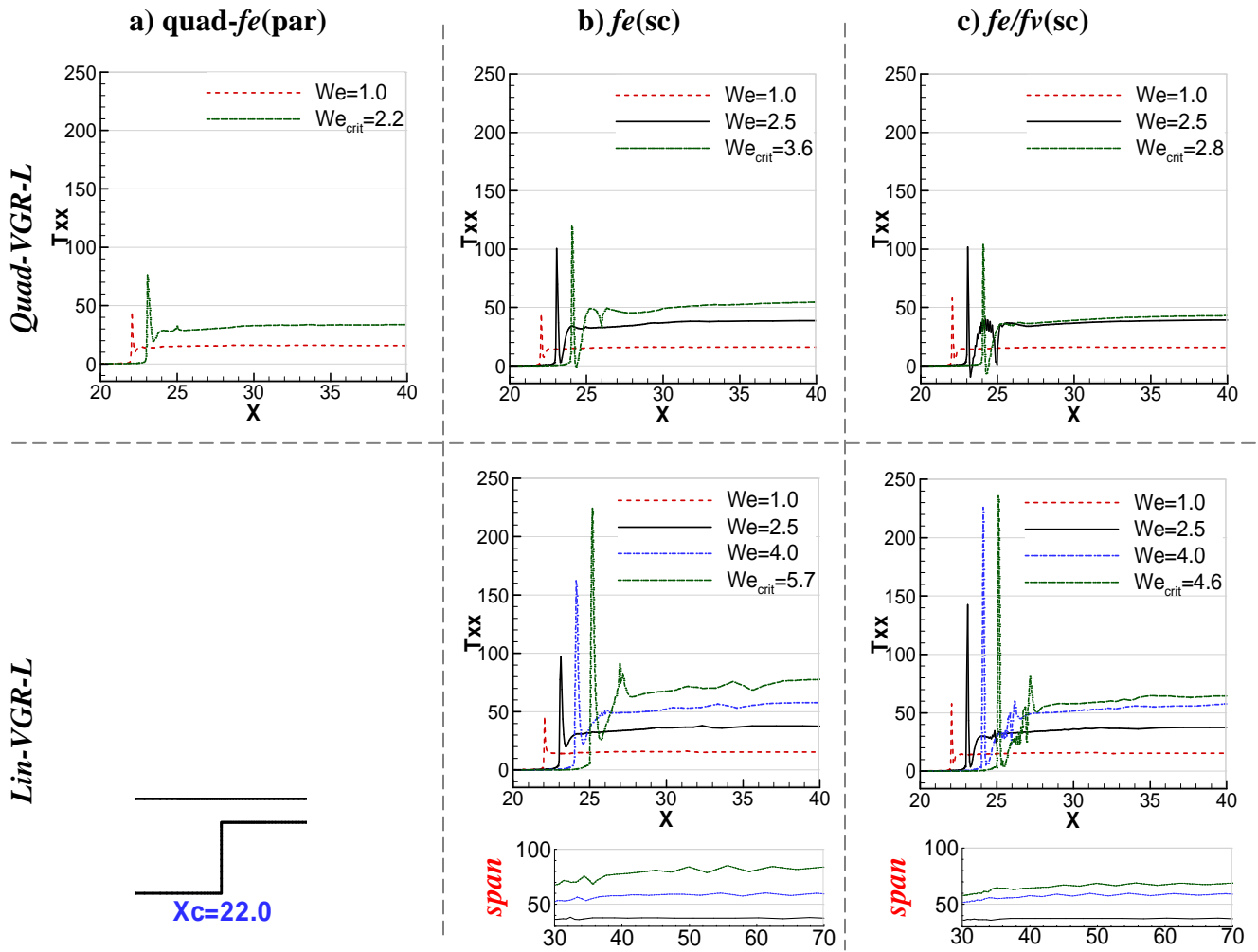


**Fig. 3.** Stress profiles, increasing  $We$ ;  $\tau_{xx}$ -profiles, downstream-wall; under (top) *Quad-VGR-L*, (bottom) *Lin-VGR-L*; a) *quad-fe(par)*, b) *fe(sc)* and c) *fe/fv(sc)*; no-area averaging

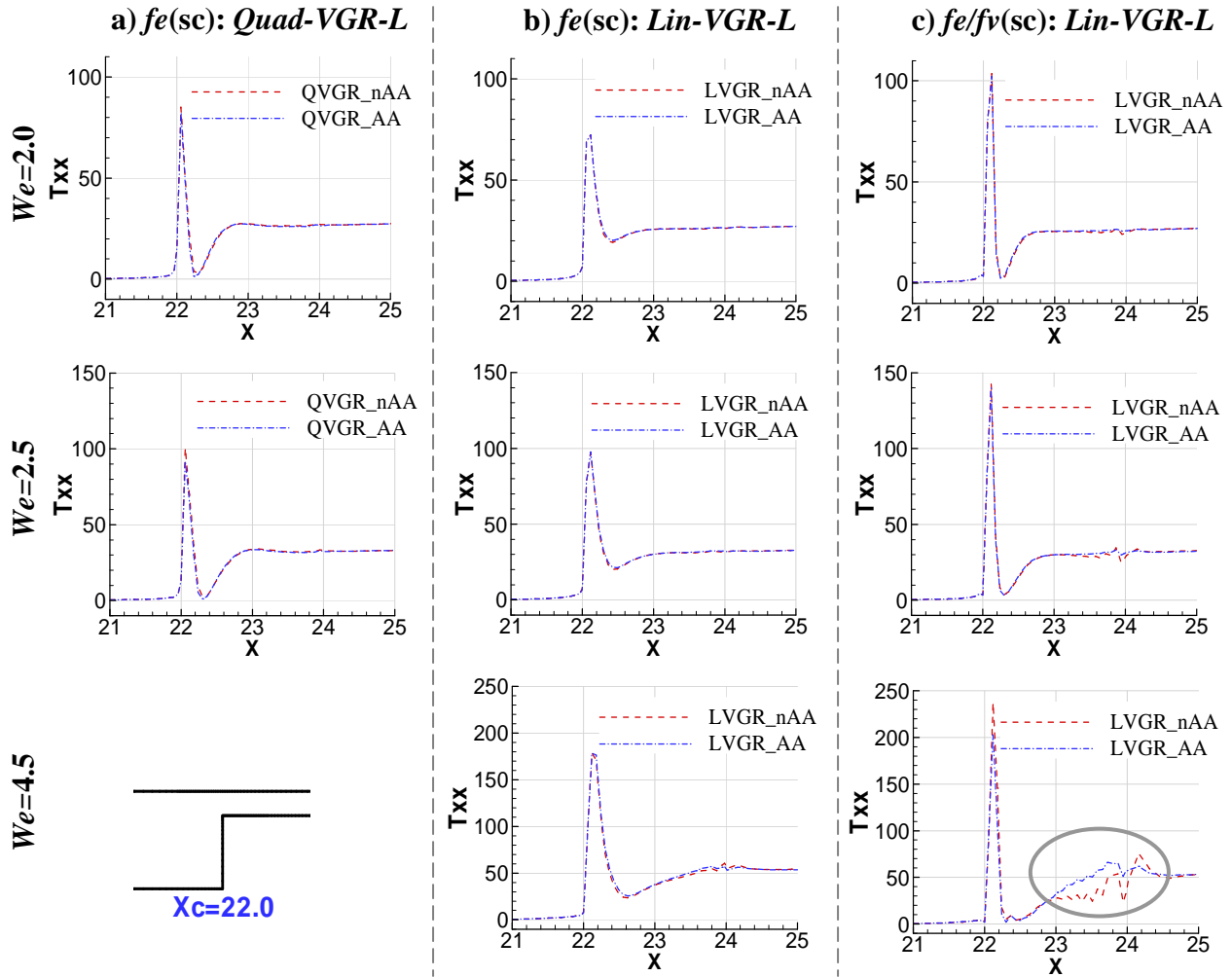


**Fig. 4.** Area-averaging (AA) vs. no-area-averaging (nAA), stress profiles,  $We=2.0, 2.5$  and  $4.5$ ;  $\tau_{xx}$ -profiles, downstream-wall; under a)  $fe(sc)$ -*Quad-VGR-L*, b)  $fe(sc)$ -*Lin-VGR-L* and c)  $fe/fv(sc)$ -*Lin-VGR-L*

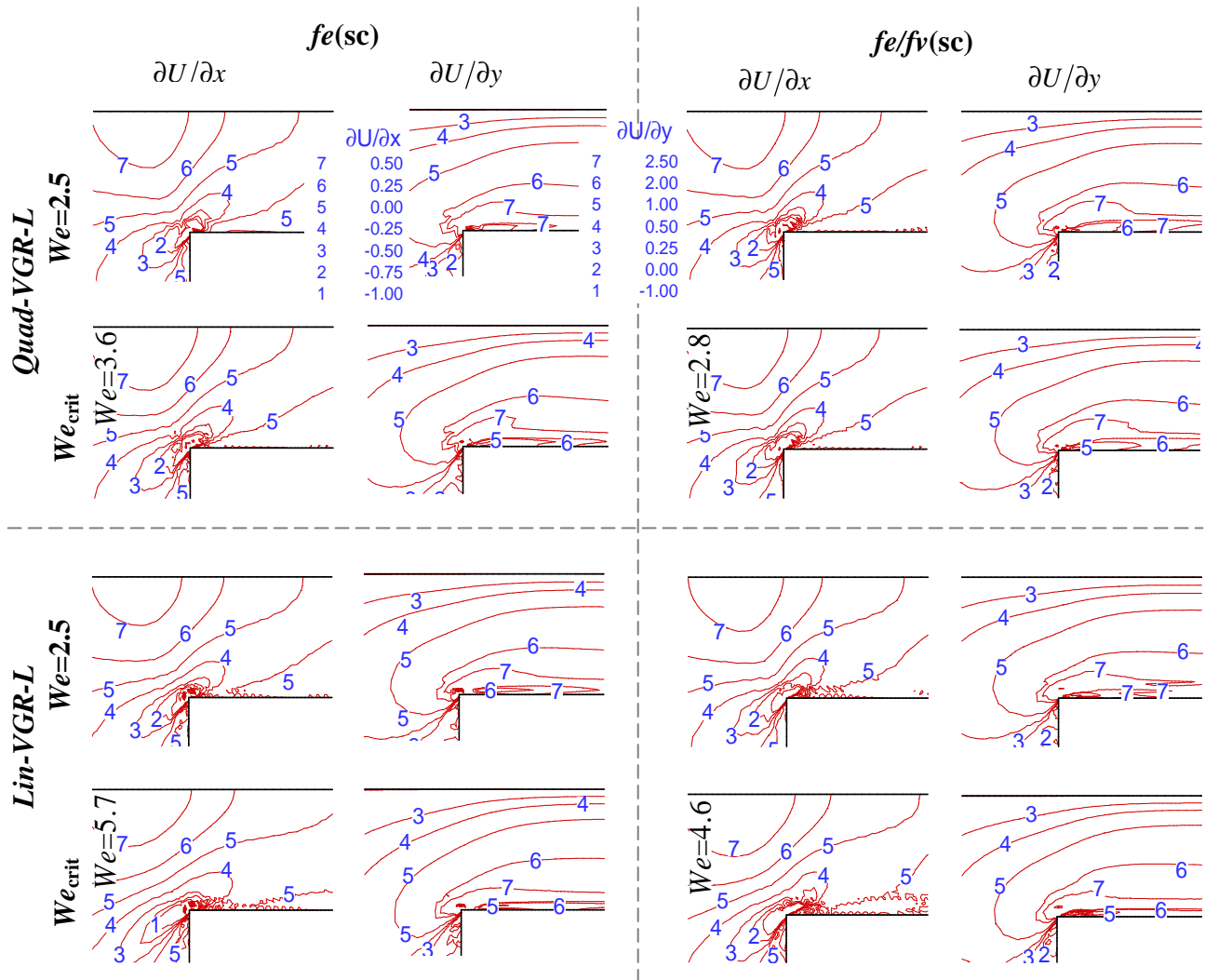


**Fig. 5.** Velocity-gradient fields,  $We=2.5$ ,  $We_{crit}$ ; (top) *Quad-VGR-L*, (bottom) *Lin-VGR-L*; (left)  $f_e(sc)$  and (right)  $f_e/f_v(sc)$

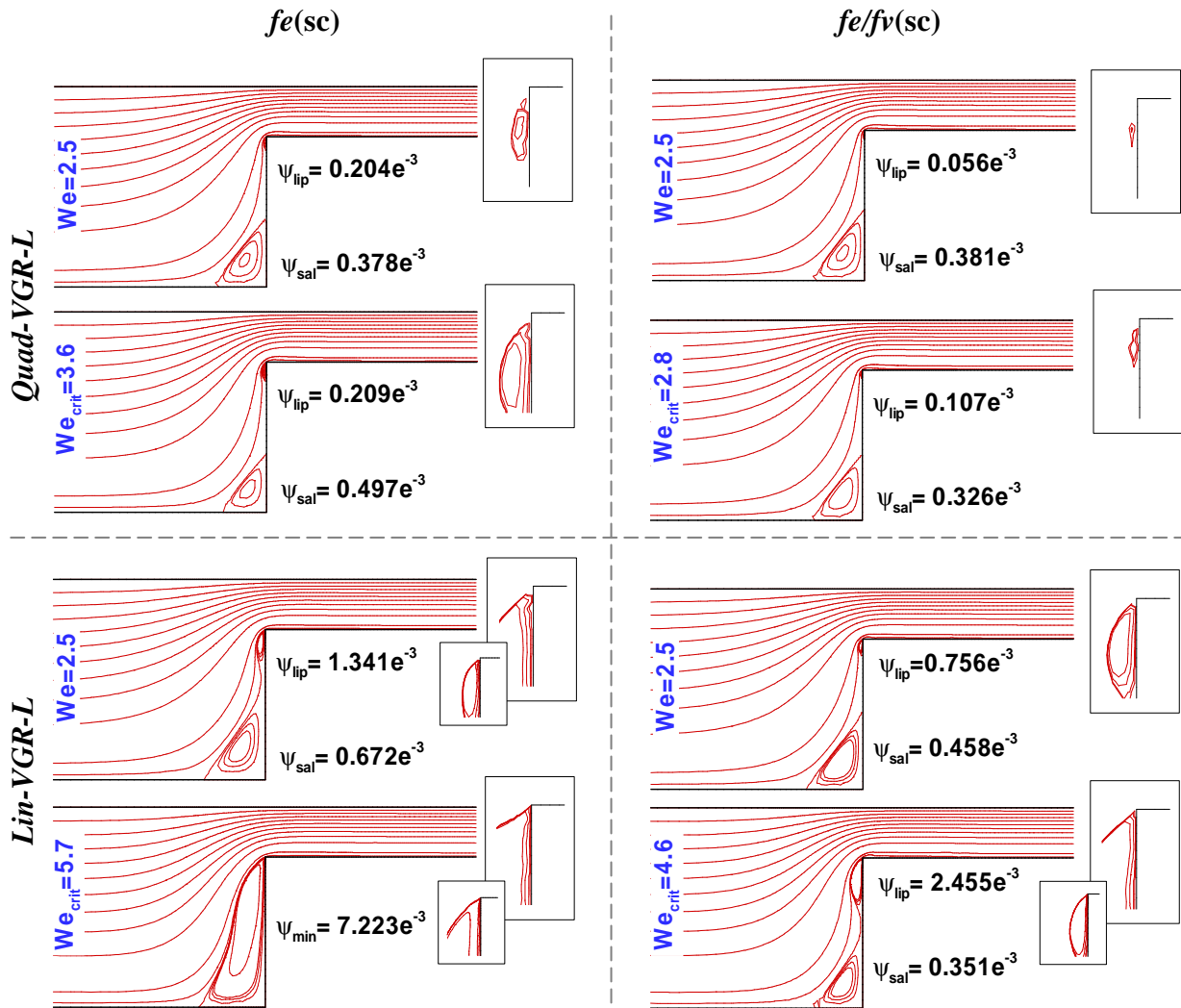


**Fig. 6.** Vortex behaviour, increasing  $We$ ; (top) *Quad-VGR-L*, (bottom) *Lin-VGR-L*; (left)  $fe(sc)$  and (right)  $fe/fv(sc)$

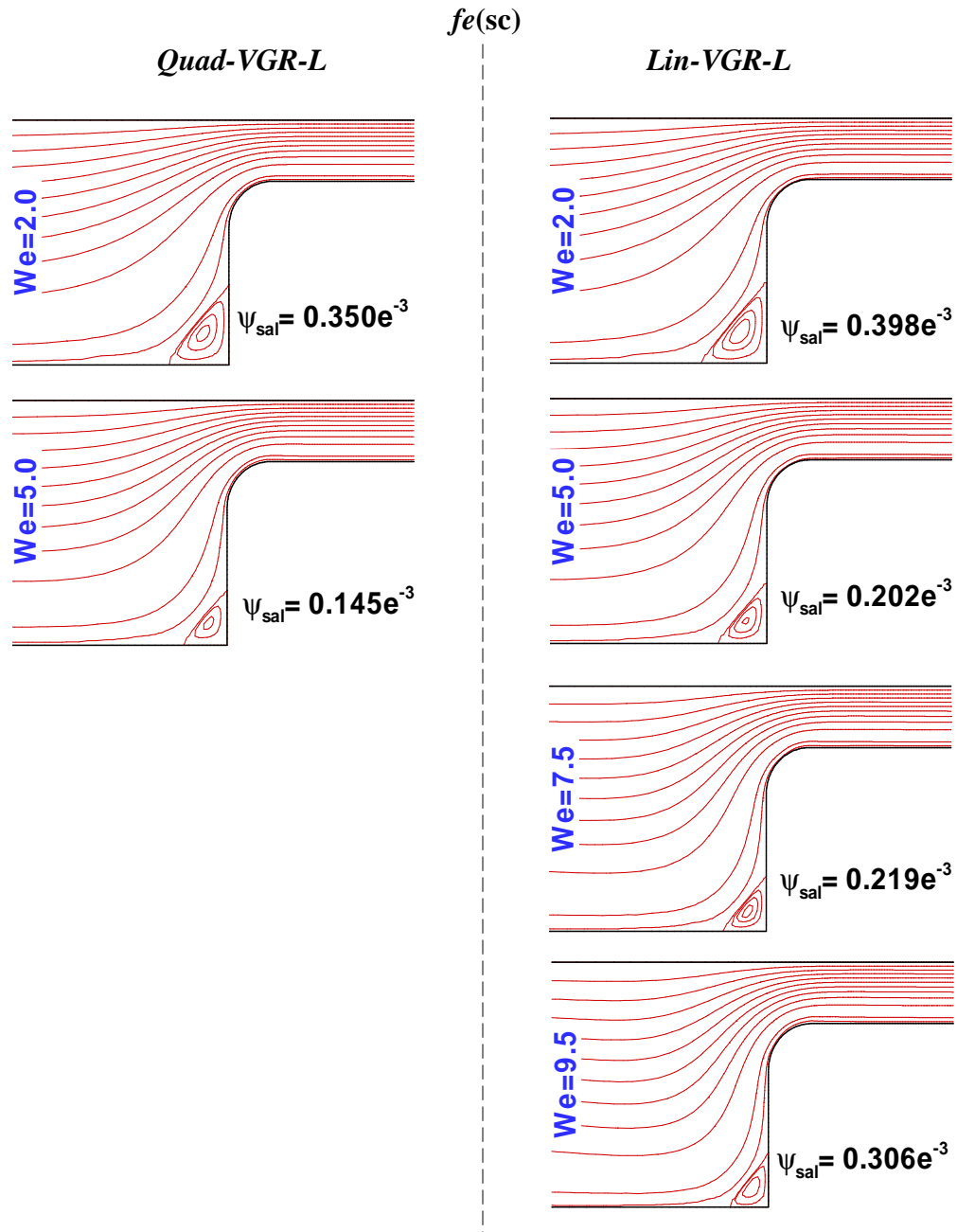


**Fig. 7.** Vortex behaviour, increasing  $We$ ; (left) *Quad-VGR-L*, (right) *Lin-VGR-L*; *fe(sc)*; rounded-corner contraction

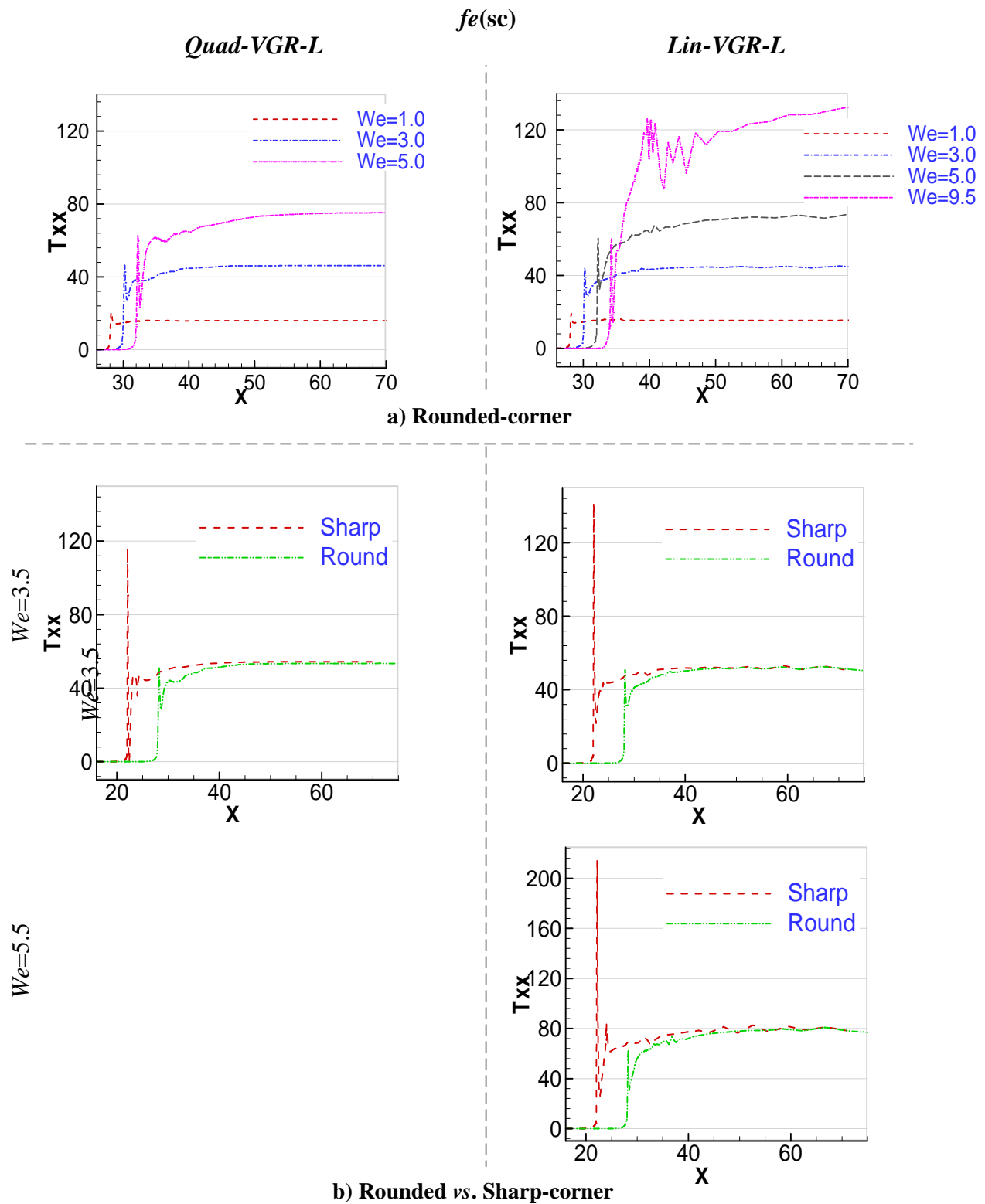


**Fig. 8.** a) Stress profiles, increasing  $We$ ;  $\tau_{xx}$ -profiles, downstream-wall; under (left) *Quad-VGR-L*, (right) *Lin-VGR-L* with zoom window; b) comparison of  $\tau_{xx}$ -profiles sharp and rounded corner; under (left) *Quad-VGR-L*, (right) *Lin-VGR-L* at (top)  $We=3.5$ , (bottom)  $We=5.5$ ;  $fe(sc)$ ; rounded-corner contraction

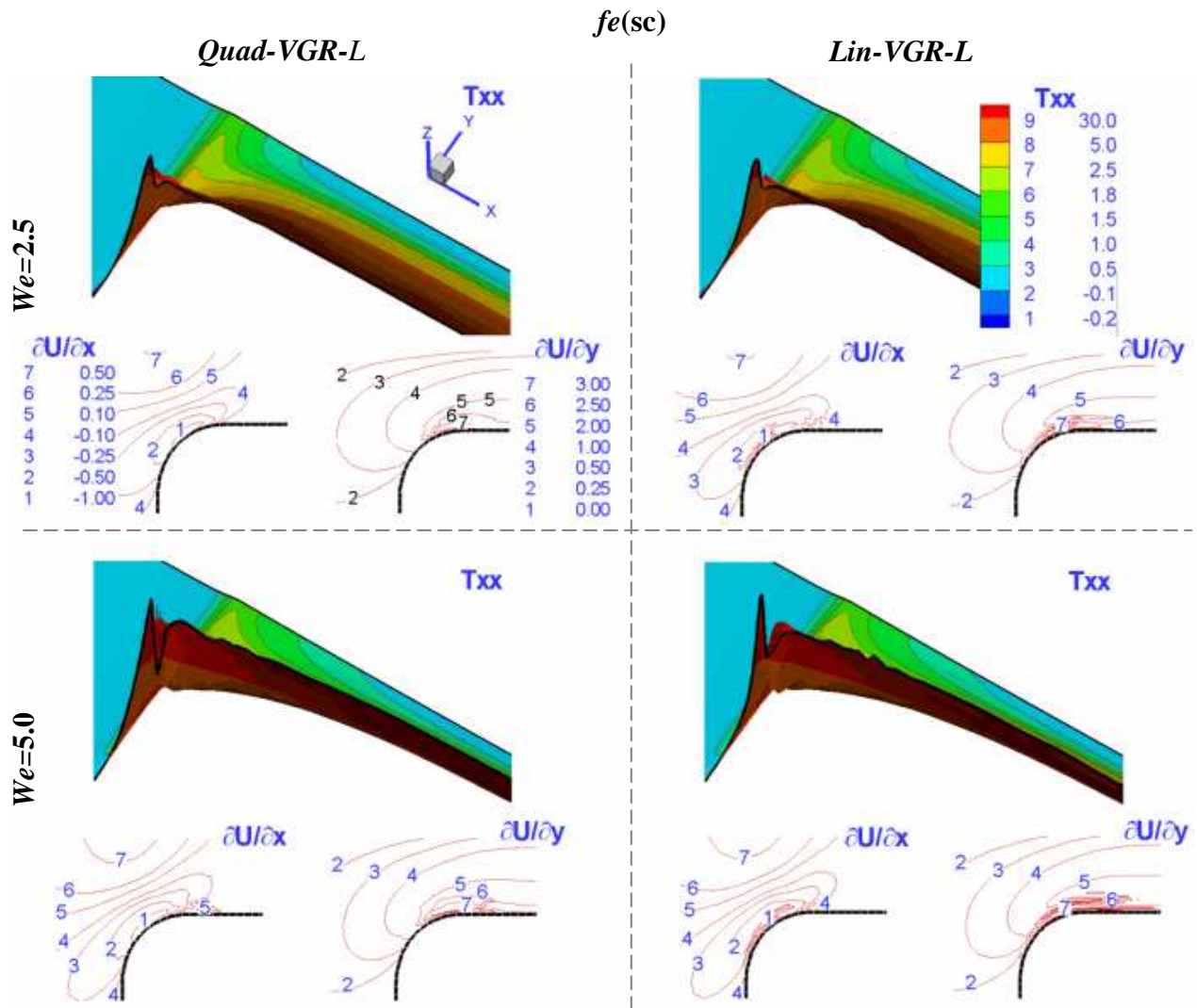


**Fig. 9.** Stress and velocity-gradient fields, (top)  $We=2.5$  and (bottom)  $We=5.0$ ;  $fe(sc)$ ; under (left) *Quad-VGR-L*, (right) *Lin-VGR-L*; rounded contraction

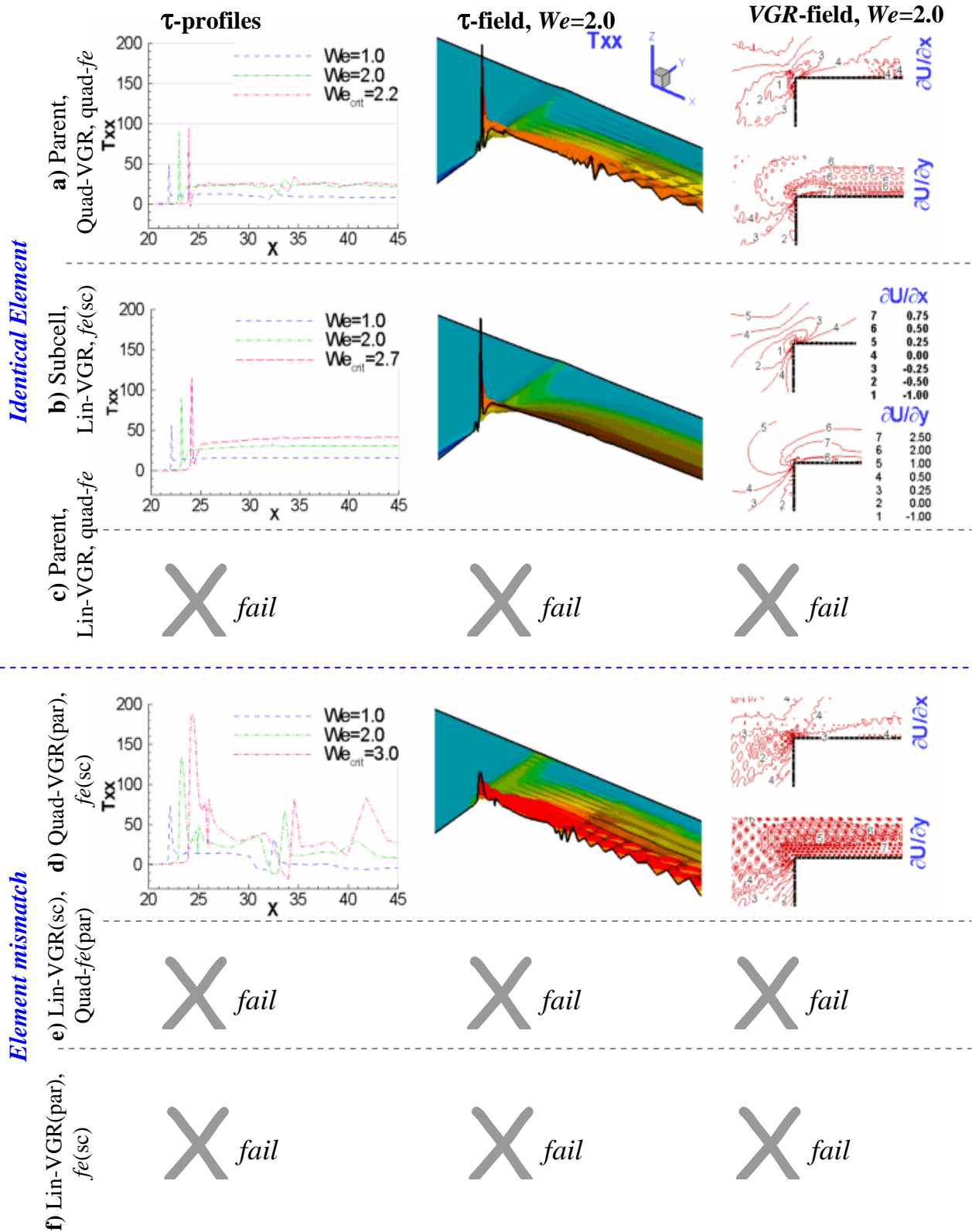


**Fig. 10.** Stress profiles, increasing  $We$ ; stress and velocity-gradient fields,  $We=2.0$ ; under identical element-base, a) *Quad-VGR-G(par)*, *quad-fe(par)*, b) *Lin-VGR-G(sc)*, *fe(sc)*, c) *Lin-VGR-G(par)*, *quad-fe(par)*; element mismatch, d) *Quad-VGR-G(par)*, *fe(sc)*, e) *Lin-VGR-G(sc)*, *quad-fe(par)*, f) *Lin-VGR-G(par)*, *fe(sc)*; Miter=5

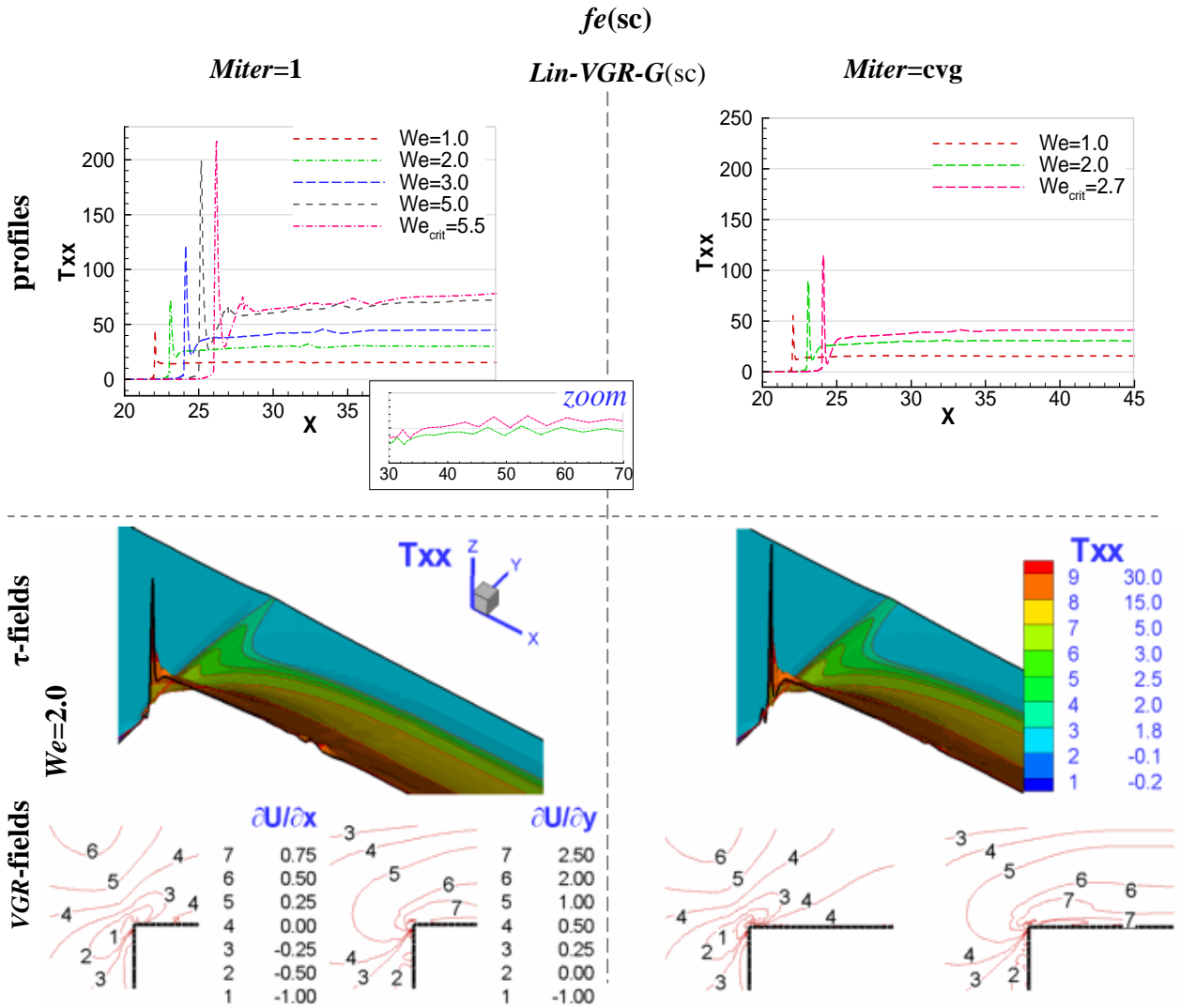


**Fig. 11.** Stress profiles, increasing  $We$ ; stress and velocity-gradient fields,  $We=2.0$ ;  $fe(sc)$ ,  $Lin-VGR-G(sc)$ ; under (left)  $Miter=1$ , (right)  $Miter=converge$

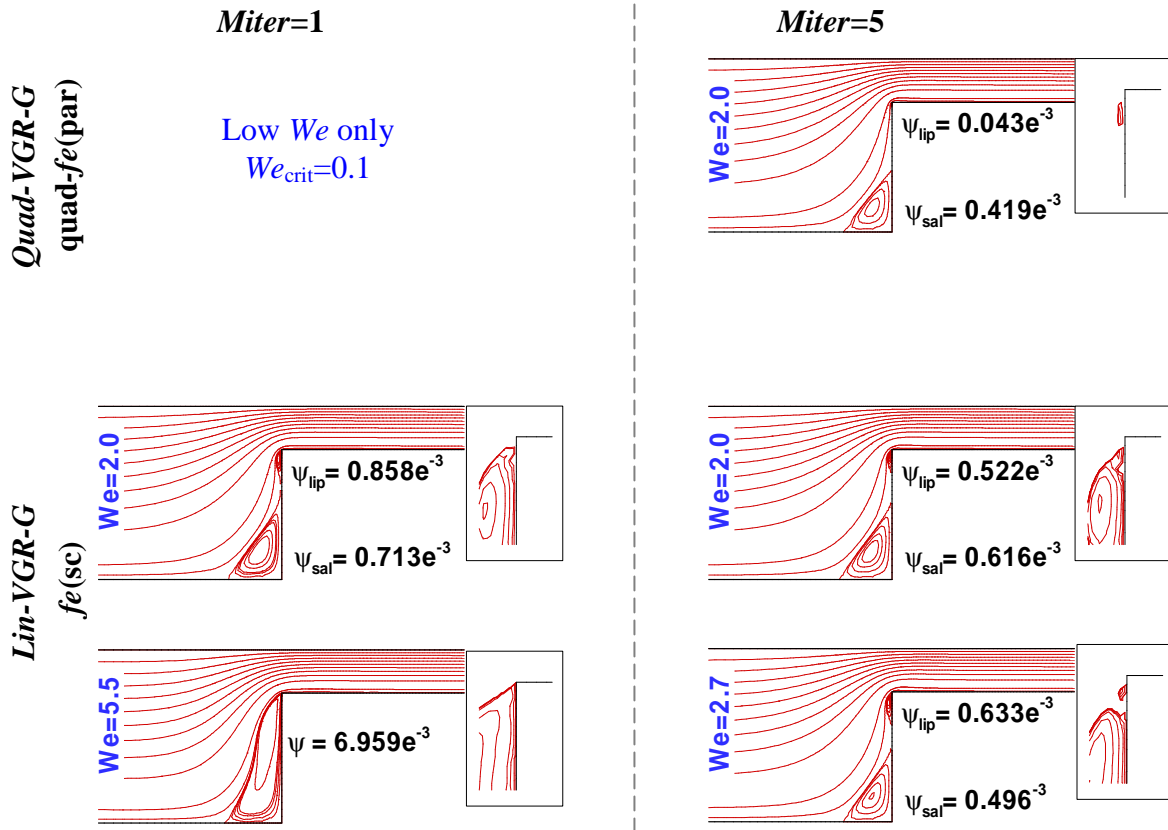


**Fig. 12.** Vortex behaviour, increasing  $We$ ; (top) *quad-fe(par)*, *Quad-VGR-G*, (bottom) *fe(sc)*, *Lin-VGR-G*; under (left)  $Miter=1$ , (right)  $Miter=5$

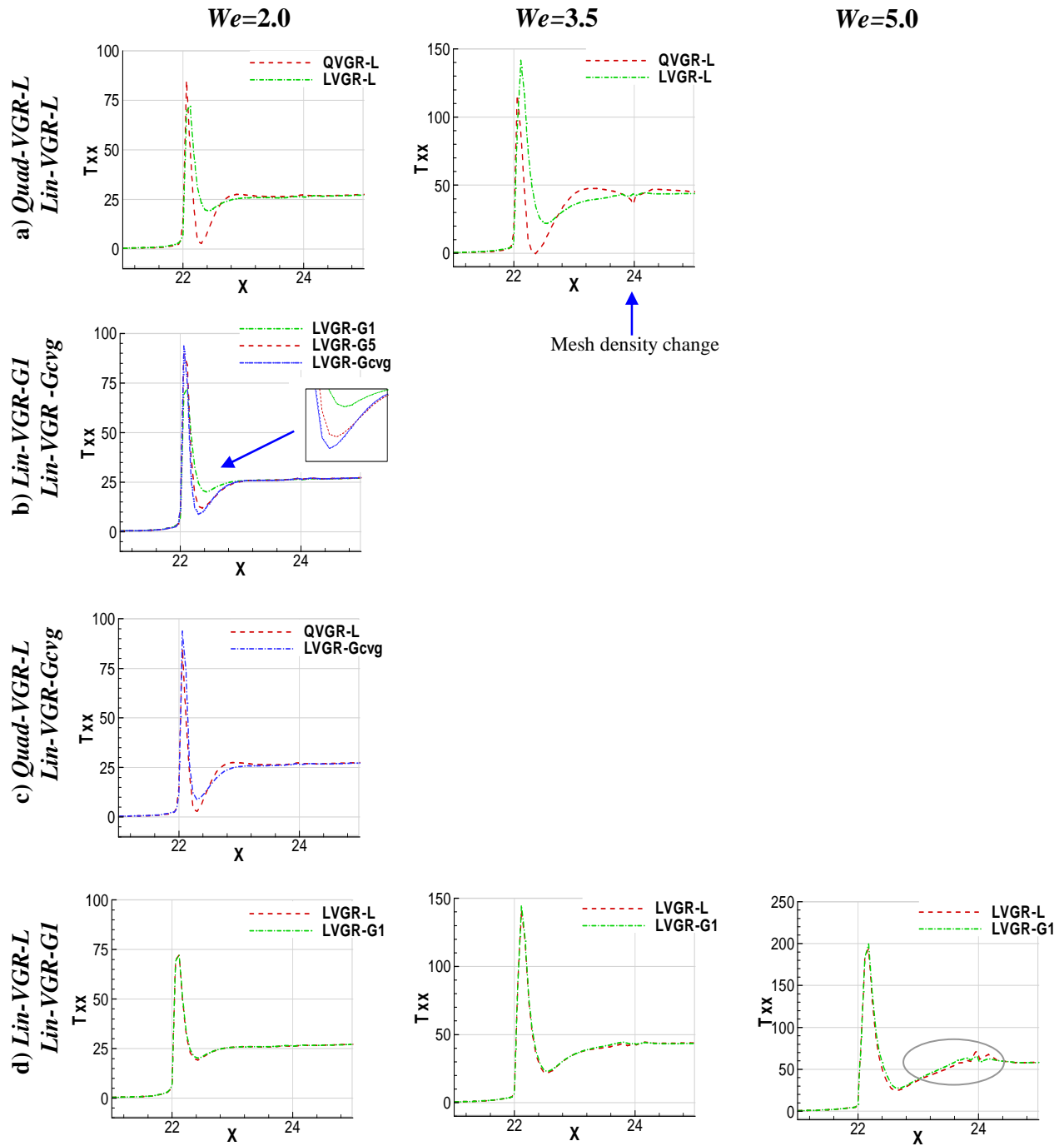


**Fig. 13.** Various VGR-treatments,  $fe(sc)$ , stress profiles,  $We=2.0, 3.5$  and  $5.0$ ;  $\tau_{xx}$ -profiles, downstream-wall; under a) *Quad-VGR-L/Lin-VGR-L*, b) *Lin-VGR-G1/Lin-VGR-Gcvg*, c) *Quad-VGR-L/Lin-VGR-Gcvg*, d) *Lin-VGR-L/Lin-VGR-G1*

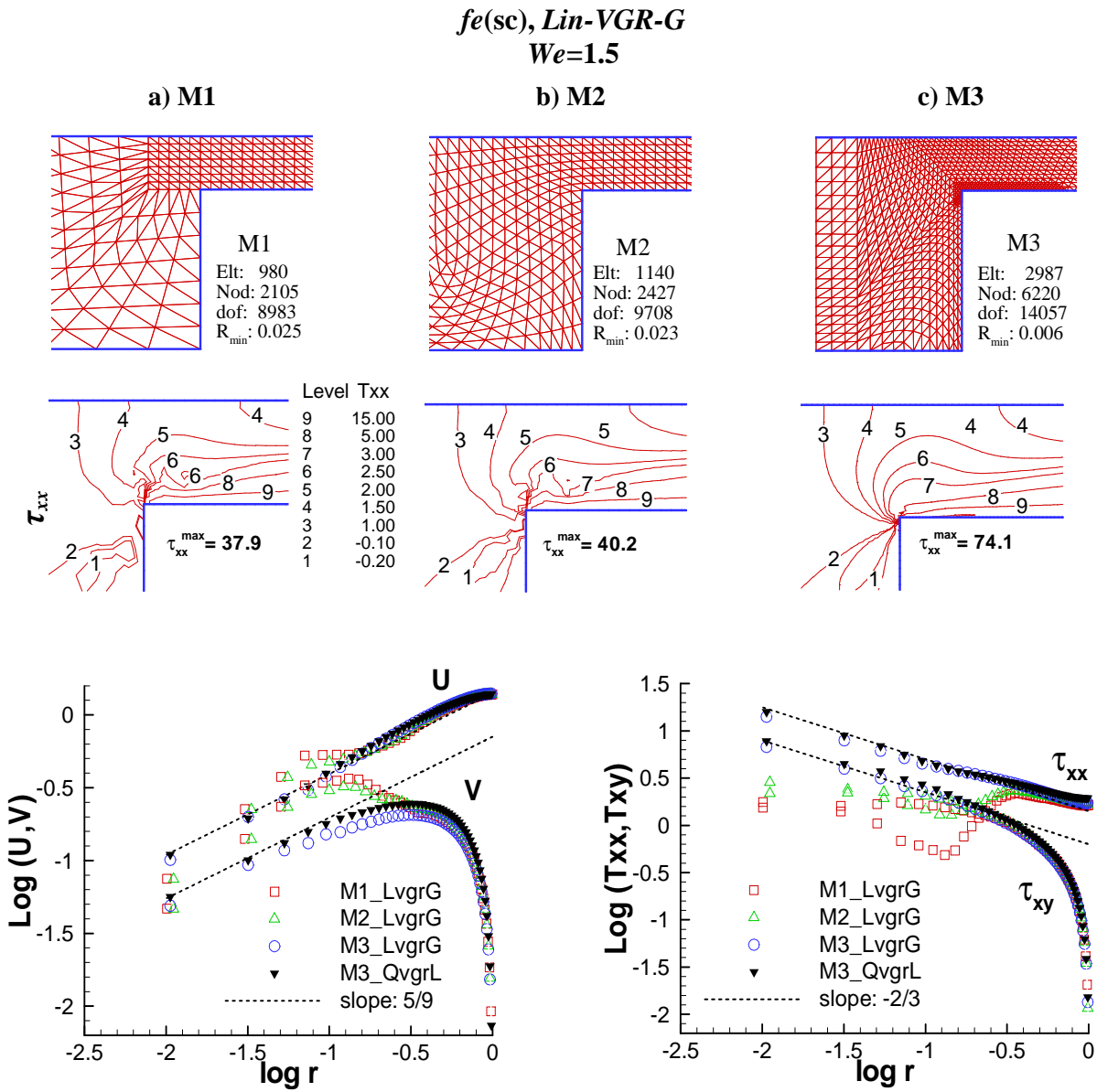


**Fig. 14.** Mesh refinement, *fe(sc)-Lin-VGR-G*, *We=1.5*; (top)  $\tau_{xx}$  and  $\partial U/\partial x$ -contour fields, a) mesh M1, b) M2 and c) M3; (bottom) asymptotic behaviour near re-entrant corner, (left) velocity (U,V), (right) stress ( $\tau_{xx}, \tau_{xy}$ ), different meshes M1-M3